Volume 13
Number 29
7 August 2025
Pages 8573–8942

Journal of Materials Chemistry B

Materials for biology and medicine

rsc.li/materials-b

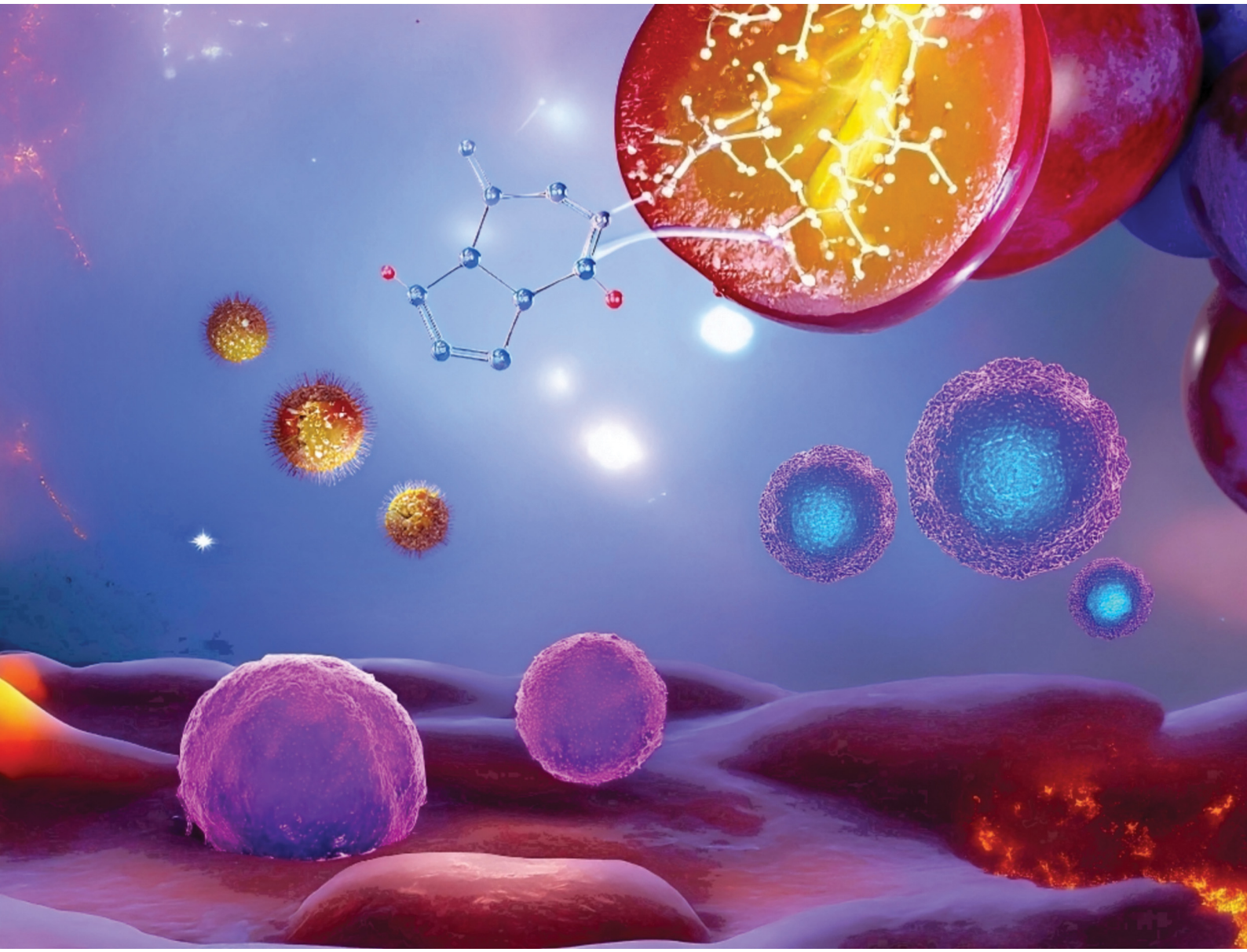

ISSN 2050-750X

ROYAL SOCIETY OF CHEMISTRY

PAPER

Kattesh V. Katti *et al.*

Immunomodulatory and tumor-targeting palladium nanoparticles functionalized with resveratrol *via* green nanotechnology: synthesis, mechanisms, and *in vivo* therapeutic evaluation

Journal of Materials Chemistry B

ROYAL SOCIETY OF CHEMISTRY

PAPER

View Article Online
View Journal | View Issue

Cite this: J. Mater. Chem. B, 2025, 13, 8683

Immunomodulatory and tumor-targeting palladium nanoparticles functionalized with resveratrol *via* green nanotechnology: synthesis, mechanisms, and *in vivo* therapeutic evaluation

Velaphi C. Thipe,[ab] Alice Raphael Karikachery,[b] Kavita Katti[bc] and Kattesh V. Katti*[bcdef]

This paper reports an innovative green nanotechnology approach utilizing electron-rich resveratrol, abundantly available in grape skin, to transform the palladium salt into biocompatible and tumor-specific resveratrol functionalized palladium nanoparticles (Res-PdNPs). This 'zero carbon emission' process affords four types of nanoparticles: Res-PdNPs 1–4, wherein the phytochemical serves dual roles of a reductant as well as a nanoparticle stabilizer through the creation of a phytochemical corona. Complete characterization has allowed selection of Res-PdNP-4 (zeta potential: −40 ± 3 mV; TEM core size: 24 ± 3 nm), with excellent *in vitro* stability, as the best candidate for further cancer therapeutic applications as elucidated through detailed *in vivo* investigations. Immunomodulatory features of Res-PdNPs suggest that they target and modulate the primary signaling pathway NF-κB, thus opening new precision medicine therapeutic opportunities for using functionalized PdNPs in treating cancer and various other inflammatory diseases. The innate relationship between NF-κB signaling and macrophage activation has been probed by investigating the ability of Res-PdNPs to target the pro-tumor M2 macrophage with concomitant re-education to the anti-tumor M1 phenotype using RAW 264.7 macrophages derived from murine cells. The immunomodulatory characteristics of this nanoceutical have been corroborated through excellent therapeutic efficacy data in prostate tumor bearing SCID mice administered with Res-PdNPs at various doses. It is highly significant that Res-PdNPs showed selective toxicity to tumor cells and minimal/no toxicity to normal cells. This is in sharp contrast to the FDA approved cancer therapy drugs cisplatin and etoposide, which showed indiscriminate severe toxicity to both normal and tumor cells. The vital role of green nanotechnology in oncology is described through compelling experimental results.

Received 18th March 2025,
Accepted 19th May 2025

DOI: 10.1039/d5tb00620a

rsc.li/materials-b

Introduction

Over the last three decades, we have demonstrated the unprecedented utility of the principles of nanotechnology in the design and development of molecular imaging and therapeutic agents.[1–27] Extensive research has allowed us to engineer a variety of nanoparticles with a myriad of functionalities, enabling facile penetration and probing into various normal and cancerous cellular domains for molecular imaging and therapy of various diseases at cellular levels.[28–30] In the rapidly expanding research endeavours of utilizing metallic and a myriad of non-metallic nanoparticles in medicine, functionalized gold nanoparticles continue to play pivotal roles in the design and development of disease-specific and targeted nanomedicine agents.[8,10,12,31–33] Medical applications of nanotechnology continue to capitalize on a pivotal scientific concept that the nanoparticulate surface provides an abundance of highly active surface atoms, which serve as highly reactive sites for the incorporation of specific drugs—therapeutic or diagnostic imaging probes—thus resulting in amplification of both diagnostic and therapeutic capabilities, which are hard to conceptualize through traditional macro-pharmaceuticals.[23,25,34–48] Surface atoms also allow incorporation of multitudes of signatures of similar or disparate therapeutic/diagnostic probes on individual nanoparticles, thus augmenting scientific reality for enhancing therapeutic or diagnostic payloads

[a] Department of Chemistry, University of Missouri, Columbia, MO, 65211, USA
[b] Institute of Green Nanotechnology and Cancer Nanotechnology, Department of Radiology, University of Missouri, Columbia, MO, 65212, USA. E-mail: kattik@health.missouri.edu
[c] Indus University, Ahmedabad, Rancharda, Via, Shilaj, Gujarat 382115, India
[d] Departments of Physics, Medical Pharmacology and Physiology, University of Missouri, Columbia, MO, 65211, USA
[e] University of Missouri Research Reactor (MURR), University of Missouri, Columbia, MO, 65212, USA
[f] Department of Biotechnology and Food Technology, University of Johannesburg, Doornfontein, 2028, South Africa

that are generally un-achievable using traditional non-nanotechnology approaches. This multiplexing approach has shown practical implications in selective and enhanced uptake of drugs at disease sites (for example within cancer cells), thus minimizing toxic off-target effects on normal cells.[9,11,12,14,30,49–54]

In order to minimize or completely eliminate the intervention of toxic chemicals, in the design and development of nanoparticles, we have conceptualized the use of green nanotechnology approaches, wherein phytochemicals from plants, rather than human made toxic chemical reducing agents, would serve as reservoirs of electrons for transforming metallic precursors of gold (and other metals) into disease specific functionalized nanoparticles.[9,10,12–14,33] Herbal-based pharmaceuticals are of considerable societal importance, because the World Health Organization (WHO) has forecast that over 80% of the world's population will utilize some type of herbal holistic medicine in their health care.[55,56] One of the major impediments in achieving this important objective of utilizing phytochemical-based herbal medicinal agents is their suboptimal bioavailability at tolerable doses. This perennial scientific reality continues to serve as an unresolved stumbling block in translating promising phytochemical-based discoveries from cell culture and animal models into clinically effective medications for treating human diseases.[57] Recently, we have demonstrated that incorporating tumor cell-specific phytochemicals into nanoparticles provides numerous advantages including: (i) receptor-mediated increased cellular uptake with consequent higher differential uptake efficiency in target cells (or tissue) *versus* normal cells (or tissue) and (ii) enhanced permeation and retention effects in disease cells/tissues, resulting in overall decreased toxicity.[15,25,38]

Interestingly, combination of gold metal and phytochemicals has been employed in the Indian holistic Ayurvedic Medicine for over 5000 years.[58–61] However, green nanotechnology approaches for engineering ayurvedic drugs have not been scientifically validated to date. In this context, our green nanotechnology strategy of encapsulating phytochemicals onto gold nanoparticles, serendipitously, offers an integrative momentum to merge the best of two worlds: five-thousand-year-old Ayurvedic holistic medicine with scientifically rigorous green nanotechnology—all aimed at enhancing global acceptability of Ayurvedic medicine. Our innovative scientific approach where we demonstrated, for the first time, the scientific intervention of green nanotechnology to transform and enhance the effectiveness of holistic herbal ayurvedic medicines was recently recognized by the United States Patents and Trademarks office, by issuing the first ever global patent, under a new medical terminology referred to as 'Nano Ayurvedic Medicine'.[9,54] Our recent successful clinical trial outcomes in treating triple-negative breast cancer patients using a new Nano Ayurvedic Medicine agent, comprising Mangiferin-conjugated gold nanoparticles (MGF-AuNPs), have provided credible scientific impetus to consider other types of metallic nanoparticles as innovative phytochemical-embedded delivery vehicles.[9] In our prior study, we developed resveratrol-conjugated AuNPs and demonstrated that increasing the resveratrol corona around AuNPs enhanced anticancer efficacy.[33] This earlier work established that a dense resveratrol corona synergized with a gold nanocarrier can improve therapeutic outcomes. However, AuNPs present certain limitations that prompted us to explore palladium as an alternative core: gold's surface chemistry is relatively inert, often requiring strong anchors to attach functional molecules, and drug release from AuNPs can be suboptimal due to overly tight binding or lack of stimulus-responsiveness. In the current study, we turned to PdNPs with the hypothesis that palladium's anomalous electronic configuration and surface properties could overcome these limitations and offer novel drug-loading and delivery characteristics.

Palladium's electronic configuration ($[Kr]\ 4d^{10}$) is indeed unusual and gives rise to distinctive surface chemistry. Unlike gold's filled $5d^{10}\ 6s^1$ configuration, elemental palladium has a fully filled d-band and no outer s-electron. This influences how molecules interact with PdNP surfaces. In terms of hard–soft acid–base (HSAB) theory, palladium is considered a relatively soft Lewis acid (especially in comparison to the predominantly hard oxygen-donor groups of polyphenolic phytochemicals). As a result, Pd surfaces bind phytochemical molecules in a weaker, more reversible fashion. In practical terms, this means that a phytochemical like resveratrol can associate with a PdNP surface without forming extremely strong or irreversible bonds, in contrast to gold surfaces that often require covalent attachments (*e.g.* Au–S bonds) or extensive capping agents for stable functionalization. The weaker coordination of phytochemicals on Pd (consistent with HSAB principles for soft Pd(II) preferring softer donor atoms) is advantageous for drug delivery: it allows the phytochemical to detach under the right conditions (such as acidic pH or intracellular glutathione), enabling controlled release at the target site.

Furthermore, palladium's unique d-electron characteristics confer catalytic properties that are absent in inert gold. Palladium can engage in π-bond interactions and catalysis on its surface resulting in antioxidative properties, such as catalase and superoxide dismutase activities,[62] while our focus is on delivery; this means that PdNPs could, for example, activate prodrugs or modulate the tumor microenvironment.

In addition, PdNPs have a broad and strong optical absorption extending into the near-infrared (NIR) region, which is optimal for deep tissue penetration. They efficiently convert NIR light into heat, enabling photothermal therapy (PTT). Therefore, a PdNP–phytochemical conjugate could thus serve as a dual-mode therapy: delivering a phytochemical drug and concurrently enabling PTT upon NIR laser irradiation.[63–65] The biocompatibility of palladium metal offers burgeoning opportunity toward the development of tumor specific biocompatible palladium nanoparticle-based nanomedicine agents—akin to numerous gold metal-based green nanotechnologies, which have resulted in a myriad of cancer imaging and therapeutic agents.[12,13,31,33,51,66,67]

Green nanotechnology approaches are particularly significant because plant-based phytochemicals are abundantly available, economically viable and considered generally safe for food and in pharmaceuticals. Therefore, the surface conjugation of tumor-specific phytochemicals presented new opportunities for

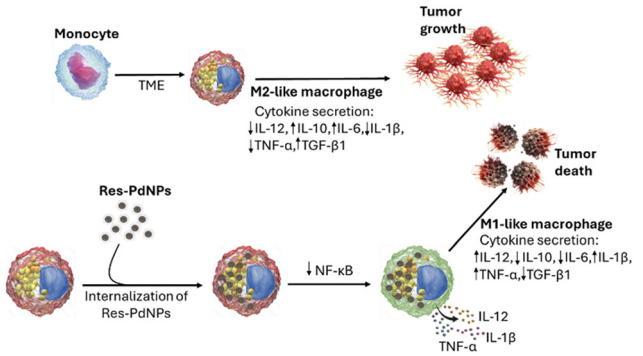

Scheme 1 Targeting ability of Res-PdNPs towards the tumor microenvironment (TME) and their ability to reprogram the M2 to the M1 macrophage phenotype.

exploring surface conjugation kinetics of palladium atoms. The objective of overarching was to explore conjugations and loading of anticancer phytochemical compounds, in their nascent forms, onto the palladium nanoparticulate surface to achieve effective drug delivery into tumor cells.

Herein, we report green nanotechnology approaches, which have led to the discovery of a series of new palladium nanoparticle-based therapeutic agents. This new nanomaterial is derived from a phytochemical called resveratrol (Res), which is abundantly present in black grape skin. The purpose of this article is to provide a conceptual overview of a new immunotherapeutic agent, derived through green nanotechnology, incorporating therapeutic phytochemicals onto well-defined palladium nanoparticles for use in prostate cancer therapy (Scheme 1). We present, herein, full details of our experimental findings on: (i) production and full characterization of nanoparticles of palladium encapsulated with the resveratrol phytochemical to create a new generation of cancer therapy nanomedicine agents capable of delivering potent doses of both palladium nanoparticles and the anti-tumor resveratrol selectively to tumor cells; (ii) targeting pro-tumor M2 macrophages, an important component within the tumor microenvironment, with concomitant re-education into the anti-tumor M1 phenotype through induction of macrophage tumoricidal activity; (iii) mechanism of cell death proving immunomodulation through targeting cell signaling pathways as well as through targeting the tumor microenvironment and finally (v) *in vivo* therapeutic efficacy investigations of the Res-functionalized palladium-based nanomedicine agent in prostate tumor bearing severe combined immunodeficient (SCID) mice. The overall implications of this 'zero carbon emission'-based green nanotechnology approach in oncology are discussed.

Materials and methods

Materials

Resveratrol, sodium tetrachloropalladate(II), gum arabic (GA), and the tetrazolium dye 3-(4,5-dimethyl thiazol-2-yl)-2,5-diphenyl tetrazolium (MTT) were purchased from Sigma (St. Louis, MO, USA). RPMI, DMEM, fetal calf serum, 1× Hanks' balanced salt solution (HBSS), TrypLE, trypan blue, DAPI (4′,6-diamidino-2-phenylindole), wheat germ agglutinin Alexa Fluor™ 488 (WGA-AF 488) and wheat germ agglutinin Alexa Fluor™ 680 conjugates (WGA-AF 680), and the laminin receptor antibody ($MLuC_5$) were purchased from Thermo Fisher Scientific, (Waltham, MA, USA). Chemotherapeutic drugs cisplatin and etoposide were obtained from Tocris Bioscience (Minneapolis, MN, USA). Recombinant human RANKL protein (Active) (ab9958) was obtained from Abcam, USA. Phospho-NF-κB p65 (Ser536) (93H1) and rabbit mAb (Alexa Fluor®488 conjugate) kits were purchased from Cell Signaling Technology, USA. Enzyme-linked immunosorbent assay (ELISA) Invitrogen kits, Tumour Necrosis Factor alpha (TNF-α) (88-7324), Transforming growth factor beta 1 (TGF-β1) (88-8350), Interleukin-1 beta (IL-1β) (88-7013), Interleukin-6 (IL-6) (88-7064), Interleukin-10 (IL-10) (88-7105), and Interleukin-12 p70 (IL-12) (88-7121), were obtained from Thermo Fisher Scientific (Waltham, MA, USA). Double distilled water was used throughout the experiment.

Cell lines. The American Type Culture Collection (ATCC; Manassas, VA) provided human prostate cancer cells (PC-3: CRL-1435), primary human aortic endothelial cells (HAECs: PCS-100-011), and murine macrophage (RAW264.7: TIB-71) cell lines, which were cultured at the University of Missouri Cell and Immunobiology Core facility according to ATCC recommendations.

Characterization of nanoparticles. A UV-vis spectrophotometer (Varian Cary 50 conc, USA) was used to measure absorption. A Zetasizer Nano S90 (Malvern Instruments Ltd. USA) was utilized to determine the hydrodynamic size and zeta potential. Transmission electron microscopy (TEM) images were acquired using a JEOL 1400 TEM (JEOL, LTE, Tokyo, Japan). Elemental mapping and analysis were performed using a high-resolution TEM (HRTEM) on a FEI Tecnai G2 F30 Twin coupled with energy-dispersive X-ray spectroscopy (EDS) (FEI, Oregon, USA). The crystalline characteristics were measured using an X-ray diffraction (XRD) Rigaku Miniflex diffractometer (Rigaku Americas Corporation, The Woodlands, TX, USA). Palladium metal concentrations were determined using inductively coupled plasma mass spectrometry (ICP-MS), PerkinElmer, MA, USA. Resveratrol concentrations were determined using liquid chromatography-multiple reaction monitoring mass spectrometry (LC–MRM/MS) on the Quantiva system (Thermo Fisher Scientific, Waltham, MA). The JEOL 1400 TEM, CytoViva Nanoscale Hyperspectral Microscope coupled with a dual mode fluorescence system (CytoViva, Inc., Auburn, USA) and Leica SP8 spectral confocal microscope (Leica Microsystems, Wetzlar, Germany) were used to capture images of cellular internalization. Cell migration analysis images were acquired and quantified using CellSens Dimension Software 1.13 on an Olympus 1 × 71 fluorescence microscope (Shinjuku, Tokyo, Japan). Immunoblotting was performed using Trans-Blot Turbo Transfer equipment and images were captured using the ChemiDoc MP Imaging System (Bio-Rad Laboratories, Inc. USA).

Synthesis of resveratrol conjugated palladium nanoparticles (Res-PdNP-1). In 6 mL of double deionized (DI) water, 1.46 mM resveratrol (Res) was prepared. At room temperature, the solution was agitated for 5 min to dissolve the Res int water and obtain a clear solution. 100 μL of 0.1 M Na_2PdCl_4 was

added to the reaction mixture to form palladium nanoparticles (Res-PdNP-1). Within 15 min, the mixture changed color to brown and yielded PdNPs. For optimization, the reaction mixture was agitated for an additional 12 h. Res-PdNPs were centrifuged at 15 000 rpm at 12 °C for 15 min and kept at 4 °C for characterization.

Synthesis of resveratrol conjugated palladium nanoparticles (Res-PdNP-2). Resveratrol (Res) at a concentration of 4.38 mM was prepared in 6 mL of double deionized (DI) water. To obtain a clear solution, it was then agitated at room temperature for 5 min. This was followed by 100 μL of 0.1 M Na_2PdCl_4 addition to generate the palladium nanoparticles (Res-PdNP-2). The Res-PdNP solution was agitated for 12 h, followed by centrifugation at 15 000 rpm at 12 °C for 15 min and kept at 4 °C for analysis.

Synthesis of resveratrol conjugated palladium nanoparticles (Res-PdNP-3). 6 mL of double ionized water (DI) was added to a 20 mL vial, followed by addition of 0.003 g of gum arabic (GA) and 1.46 mM resveratrol (Res). At room temperature, the solution was agitated for 5 min, followed by the addition of 100 μL of 0.1 M Na_2PdCl_4 to form the palladium nanoparticles (Res-PdNP-3). The reaction mixture was stirred for 12 h and centrifuged at 15 000 rpm at 12 °C for 15 min and kept at 4 °C for characterization.

Synthesis of resveratrol conjugated palladium nanoparticles (Res-PdNP-4). To a 20 mL vial was added 6 mL of double ionized water (DI), followed by addition of 0.003 g of GA and 4.38 mM resveratrol (Res). The solution was stirred at room temperature for 5 min to dissolve the Res in water to get a clear solution. Then to the reaction mixture, 100 μL of 0.1 M Na_2PdCl_4 was added to produce the palladium nanoparticles (Res-PdNP-4). The color of the mixture changed to brown within 15 min and developed into homogenous PdNPs. The reaction mixture was further stirred for an additional 12 h for optimization. The Res-PdNPs were then centrifuged at 15 000 rpm at 12 °C for 15 min to remove any unreacted Res and the palladium salt and were stored at 4 °C for characterization.

***In vitro* stability analysis of Res-PdNPs.** The stability of Res-PdNPs was determined by incubating palladium nanoparticles in various biological solutions [1% NaCl, 0.5% cysteine, 0.2 M histidine, 0.5% human serum albumin (HSA), 0.5% bovine serum albumin (BSA), phosphate buffered saline at pH 5, pH 7, and pH 9 and a mixture of these solutions at equivalent volumes] in triplicates (n = 3) at 37 °C in 5% CO_2 to mimic *in vivo* conditions. DLS measurements were taken using the Malvern Zetasizer Nano-ZS90 to track the changes in the hydrodynamic size as a stability metric. These measurements were performed for a one-week period.

Quantification of resveratrol on the surface of Res-PdNPs. We assessed the amount of Res molecules attached to the surface of PdNPs using liquid chromatography-multiple reaction monitoring mass spectrometry (LC-MRM/MS) on a Quantiva triple quadrupole mass spectrometer (Thermo Fisher Scientific, Waltham, MA). A method was developed to determine MRM transitions for Res and its column retention time. Res-PdNPs were centrifuged at 16k×g for 5 min in a microcentrifuge tube and the supernatant was diluted 1 : 10 000 with an internal standard solution [30 ng mL^{-1} tolbutamide in 5% acetonitrile (ACN)/1% formic acid (FA)]. Following that, 25 μL was transferred to autosampler vials and placed in a cool (7 °C) autosampler.

The Res standard (5 μL) was injected into a C_{18} trap column (C_{18} trap, Eksigent) and the sample was eluted from the trap column and separated on a 20 cm × 75 μm inner diameter pulled-needle analytical column packed with HxSIL C_{18} reversed phase resin (Hamilton Co.) using a 500 nL min^{-1} step gradient of acetonitrile. A Thermo Scientific TSQ Quantiva triple-quadrupole mass spectrometer was connected to the Eksigent Nano 1D plus HPLC system. Conditions for the LC gradient: initial conditions were 2% B (A: 0.1% formic acid in water; B: 99.9% acetonitrile and 0.1% formic acid), followed by 2 min ramp to 90% B, which was maintained for 8 min, before being ramped back to (1 min) and maintained under (2 min) initial conditions. The run lasted a total of 10 min.

MRM conditions: 1600 V ionization voltage, 0.7 (full-width half max) resolution in Q1 and Q3, 2.5 mTorr collision gas, 200 ms dwell time. An MRM transition is composed of a precursor–fragment pair, which enables the mass spectrometer (Thermo Scientific TSQ Quantiva) to ignore all other molecules in a sample except for the Res enabling precise quantification with extremely high specificity and sensitivity. To precisely quantify the Res, the following two optimal transitions were created: Res (1.1 mM in ethanol) was diluted 1 : 1000 in 70% ACN, 0.1% FA. This solution was then examined directly (3 μL min^{-1}) for Res quantification conjugated to the surface of the Res-PdNPs.

Cellular internalization and the trafficking pathway of Res-PdNPs. The method of endocytosis of Res-PdNPs *via* cellular internalization was examined by pre-blocking the laminin receptor (67LR) overexpressed PC-3 cells. The optimal dose and incubation duration were established by treating PC-3 cells with resveratrol conjugated palladium nanoparticles (Res-PdNPs) at various time points. The cellular trafficking pathway of Res-PdNPs was further elucidated utilizing an inhibitor of laminin receptor, RPSA monoclonal antibody (MLuC5), to confirm laminin receptor-mediated endocytosis. Three different approaches were used to evaluate Res-PdNP cellular internalization: (i) CytoViva dark field fluorescence microscopy; (ii) Leica SP8 spectral confocal microscopy; and (iii) transmission electron microscopy (TEM). For the dark field and confocal microscopy examination, a sterile coverslip was used to culture PC-3 cells in 6 well plates, whereas for TEM studies, the cells were grown in the plate without a coverslip. Briefly, the PC-3 cells (8×10^5 mL^{-1}) were seeded onto 6 well plates containing RPMI medium and cultured for 24 h at 37 °C in a CO_2 incubator. PBS (control) and the MLuC5 laminin receptor antibody (10 μM; 60 min) were used to pre-incubate the cells, and the cells were then incubated at 37 °C in a CO_2 incubator. Following incubation, the cells were washed twice with 1× PBS and then incubated with Res-PdNPs (44 μM) at 37 °C in a CO_2 incubator. The following approaches were used to prepare the samples.

Confocal and dark field microscopic techniques. Following incubation, the cells were washed 5 times with 1× PBS and

fixed for 15 min in the dark with 4% paraformaldehyde (PFA). The cells were then washed 3 times with 1× Hanks' Balanced Salt Solution (HBSS) and labeled with the 2 μM wheat germ agglutinin Alexa Fluor™ 488 (WGA-AF 488) conjugate, which was incubated at room temperature in the dark for 10 min. Following incubation, the cells were washed twice with 1× HBSS and permeabilized for 5 min at room temperature with 0.2% Triton X-100. The cells were washed twice as much with 1× HBSS and the slides were stained with the DAPI nuclear dye. The cells were observed using a CytoViva Nanoscale Hyperspectral Microscope paired with a dual mode fluorescence system and the Leica SP8 spectral confocal microscope. The initial observation of the cell morphology was made followed by Res-PdNP uptake; images were captured using Dage Imaging Software and LAS X software respectively.

TEM technique. Following incubation, the cells were washed 10 times with 1× PBS, trypsinized and centrifuged into pellets, and fixed with 2% glutaraldehyde and 2% paraformaldehyde in sodium cacodylate buffer (0.1 M). Additionally, the cells were further fixed with 1% buffered osmium tetroxide in 2-mercaptoethanol buffer and dehydrated in graded acetone series before being embedded in Epon-Spurr epoxy resin. Sections were cut at a thickness of 85 nm with a diamond knife (Diatome, Hatfield PA). For organelle visualization, the slices were stained with Sato's triple lead stain and 5% aqueous uranyl acetate. The prepared samples were evaluated at the University of Missouri's Electron Microscopy Core Facility, Columbia, MO, USA, using a JEOL 1400 TEM microscope (JEOL, Peabody, Mass.) operating at 80 kV. The cytotoxicity of Res-PdNPs was investigated to determine their specific affinity for PC-3 cells and their effects on normal endothelial cells (HAECs) treated at various concentrations and time points.

Cell viability assay. The MTT assay was used to investigate the effect of Res-PdNPs on the viability of prostate cancer (PC-3) and normal human aortic endothelial cells (HAECs). 96-well plates were seeded with 100 μL per well of 5×10^4 cells per mL and the cells were cultured for 24 h at 37 °C in a CO_2 incubator with 5% CO_2. After incubation, the medium was withdrawn and the cells were treated with the Res-PdNPs, GA-PdNPs, free Res and GA at various concentrations (0, 2.7, 5.5, 11, 22 and 44 μM), respectively. Cisplatin and etoposide were employed as positive controls and the cells without treatment served as negative controls. After treating the cells at various time intervals (24, 48 and 72 h), 10 μL of MTT dye solution was added in each well and the plates were incubated for an additional 4 h to allow crystallization. After carefully removing the medium solution, 100 μL of dimethyl sulfoxide (DMSO) was added to dissolve the formazan crystals. The vitality of the cells was determined using a microplate reader (Molecular device, USA) set at 570 nm. The formula below was used to determine the percentage of viable cells:

$$\text{Cellular viability (\%)} = \frac{\text{Absorbance of the treated cells at 570 nm}}{\text{Absorbance of untreated cells at 570 nm}} \times 100\%$$

GraphPad Prism version 6.01 software was used to calculate the half-maximal inhibitory concentration (IC_{50}).

Migration assay and cellular morphology studies of Res-PdNPs against PC-3. We studied the migrastatic effect of Res-PdNPs on PC-3 cell motility inhibition. Briefly, 6-well plates were labeled to indicate the region to be imaged, and 5×10^5 cells per mL were seeded into 6-well plates and cultured for 24 h to achieve 100% confluence. A 200 μL sterile pipette tip was used to aseptically stretch the cell monolayer vertically. The media and cell detritus were aspirated carefully, and the plates were gently washed with 1× PBS solution. For 24 h, the cells were treated with the highest concentration of Res-PdNP-4 (44 μM). The cells were imaged at 1 h and 24 h after treatment using an Olympus 1X71 Fluorescence Microscope (Shinjuku, Tokyo, Japan). The stretch's area was determined using CellSens Dimension Software 1.13 and ImageJ v1.54p Software.

The effect of Res-PdNPs on NF-κB inhibition in PC-3. The cells were seeded into 6-well plates and then pre-incubated with the receptor activator of the NF-κB ligand (RANKL) to stimulate NF-κB expression (positive control); the cells were treated with Res-PdNPs without RANKL activation (negative control) and then treated with Res-PdNPs at various concentrations (25, 50, and 100 μM) for 2 h and then post-treated either with RANKL (25 ng mL^{-1}) or left untreated for 4 h. The cells were lysed, followed by electrophoresis on polyacrylamide gels and transfer to nitrocellulose membranes using the Trans-Blot Turbo Transfer System operating at 1.3 A at 25 V for 7 min. These membranes were then probed with a primary antibody for phospho-NF-κB and detected with the secondary antibody horseradish peroxidase-conjugated goat anti-rabbit IgG (1 : 1000 dilution) using the ChemiDoc MP Imaging System.

Macrophage Res-PdNP uptake studies. In a 75 cm^2 flask, RAW 264.7 macrophages were grown in DMEM + 10% FBS. To determine adhesion, 1×10^6 cells were plated overnight in 6 well plates. The cells were subsequently supplemented with fresh medium and treated for 60 min with Res-PdNPs (44 μM). The cells were labelled with 2 μM wheat germ agglutinin Alexa Fluor™ 680 conjugates (WGA-AF 680) and stained with the DAPI nuclear dye. The presence of palladium nanoparticles in cells was then determined using a Leica SP8 spectral confocal microscope.

Assessment of the immunomodulatory effects of Res-PdNPs on RAW 264.7 macrophages. Murine RAW 264.7 macrophages were maintained in DMEM enriched with 10% fetal bovine serum and gentamicin, incubated at 37 °C in a humidified atmosphere containing 5% CO_2. For the experiment, the cells were plated in multi-well dishes so that they reached roughly 70–80% confluence by the next day. They were then pre-incubated with 50 μg mL^{-1} Res-PdNPs for one hour to promote nanoparticle uptake. Following this pre-treatment, lipopolysaccharide (LPS) was introduced to a final concentration of 1 μg mL^{-1}, and the cells were incubated for an additional 4 hours to initiate an inflammatory response.

After incubation, the supernatant was carefully harvested and centrifuged at low speed to remove any cellular debris and then stored at −80 °C until further cytokine analysis. The levels of various cytokines—both pro-inflammatory (IL-1β, TNF-α, IL-6, and IL-12) and anti-inflammatory (TGF-β1 and IL-10)—were

measured using enzyme-linked immunosorbent assay (ELISA) kits following the manufacturer's protocols. Standard curves for each cytokine were generated, and optical density readings were obtained at 450 nm using a calibrated SpectraMax M2 microplate reader. All experiments were performed in triplicate to ensure statistical reliability, and the data were normalized against untreated controls to determine the modulatory impact of Res-PdNPs on LPS-induced cytokine production.

Co-culture analysis of the immunomodulatory effect of Res-PdNP treated macrophages on prostate cancer cell proliferation. PC-3 cells (1×10^5 cells per well) were plated overnight in a 6-well plate for adherence. Following that, RAW 264.7 macrophages were treated for 18–24 h with Res-PdNPs (22 μM) and labeled with a 2 μM WGA Alexa Fluor™ 680 conjugate. To avoid the direct influence of Res-PdNPs on cancer cells, the macrophages were washed twice with 1× HBSS to eliminate unbound Res-PdNPs. To differentiate and measure the proliferation of PC-3 cells, they were labeled with the 2 μM WGA Alexa Fluor™ 488 conjugate. For 72 h, macrophages were then co-cultured with PC-3 cells at the ratio of 1 : 10 (1 part of PC-3 cells to 10 parts of macrophages). The co-culture images were acquired using a Leica SP8 spectral confocal microscope.

Animal studies. All animal research with Res-PdNPs was approved by the Institutional Animal Care and Use Committees (IACUC) of the Harry S. Truman Memorial Veterans Hospital and the University of Missouri and was conducted in accordance with the Guide for the Care and Use of Laboratory Animals. Male mice with imprinting control regions-severe combined immunodeficiency (ICR-SCID) were used in the therapeutic investigations (from Taconic Farms, Hudson, New York). The mice utilized in our studies weighed between 24 and 27 g.

***In vivo* therapeutic efficacy study.** We assessed the antitumor activity of Res-PdNPs by establishing a prostate tumor model (in SCID male mice). Under inhalation anesthesia (isoflurane/oxygen), SCID male mice were subcutaneously injected with 10×10^6 PC-3 cells (suspended in 0.1 mL of sterile DPBS and Matrigel® (2 : 1, v : v) in the right hind flank. Following injection, the animals received intravenous (IV) treatment twice a week until palpable tumors developed. The mice were randomly assigned to one of three groups (n = 5/group) with no significant difference in tumor volume; the day of randomization was deemed day zero of the therapeutic study. On day 0, tumors were measured using a digital caliper and dimensions were determined as length × width × height. The first group was given 100 μL saline as the control group (n = 5). The second group received 100 μL Res-PdNP-4 (0.25 mg kg^{-1} bw) (n = 5), whereas the third group received 100 μL free Res (7 mg kg^{-1} bw) injection (n = 5). For an additional 6–7 weeks, the animals were evaluated for tumor volume, body weight and health consequences before being euthanized. A normal healthy group of mice (n = 5) that had not been experimentally manipulated served as a control for determining complete blood count (CBC) parameters (mean counts of white blood cells (WBCs), red blood cells (RBCs) as well as hemoglobin, lymphocytes, and platelets) and body weight/eating habits of the animals to investigate how well treated groups were tolerated. For roughly 6–7 weeks, all groups were examined twice weekly for body weight and tumor volume assessments. Animals were sacrificed at the conclusion of study or when tumors reached the endpoint (as determined by body weight, physical appearance, observable clinical indications, unprovoked behavior, responsiveness to external stimuli, and a tumor burden higher than 10% body weight). Tumors were subjected to histopathology analysis to determine angiogenesis. The CD31 antibody was used to stain animal tissues for angiogenesis studies.

Statistical analysis. All experimental data are shown as mean ± SEM. GraphPad Prism software was used to conduct statistical analysis using one-way analysis of variance (ANOVA). $P < 0.05$ was considered significant.

Results and discussion

Green nanotechnological architecture and characterization of Res-PdNPs

Resveratrol (3,5,4′-trihydroxy-*trans*-stilbene) is a stilbenoid containing polyphenol, which is found in abundance in a variety of fruits including grapes, blueberries, raspberries, and mulberries.[68] In continuation of our pioneering work on exploiting phytochemicals with the high antioxidant capacity—as green sources of electrons—for transforming metal salts into their corresponding phytochemical functionalized nanoparticles,[9,10,12,14,31,33,51,67] we have used resveratrol with the high antioxidant capacity both as a reducing agent and to create its robust corona on the palladium nanoparticle (Res-PdNP) surface. Antioxidant phytochemicals have the potential to act as electron reservoirs, thus allowing metals to be transformed into their corresponding nanoparticle forms. Electron paramagnetic resonance (EPR or ESR) spin trapping studies demonstrate the antioxidant capacity of this phytochemical by measuring its ability to scavenge free radicals (0.64 for resveratrol in Trolox equivalents).[69,70] Therefore, the high antioxidant capacity of resveratrol offered a unique opportunity, as an electron reservoir, to transform the palladium precursor into its corresponding nanoparticles (PdNPs). After optimizing a highly reproducible and scalable procedure, we were able to produce resveratrol-encapsulated Pd nanoparticles (Res-PdNPs) by interaction of the optimized amount of resveratrol with a Pd salt solution in aqueous medium. The excess resveratrol in the reaction mixture forms a robust encapsulation corona around Pd nanoparticles, thus eliminating the requirement for external chemical-based toxic reducing agents and stabilization agents to prevent the agglomeration of Res-PdNPs. In separate experiments, Pd nanoparticles were also stabilized using gum arabic (GA) protein—a dietary fiber-derived protein with a glycoprotein and polysaccharide structural motif that has been approved by the Food and Drug Administration (FDA) as well as by the World Health Organization (WHO) for use in pharmaceuticals and foods.[12,67,71] These green nanotechnology techniques exemplify 'zero carbon footprint' processes because no other human-derived toxic chemicals are employed in the overall production schemes as well as for the stabilization of Res-PdNPs. Green

Table 1 Physicochemical properties of Res-PdNPs

Sample	Hydrodynamic size (nm)	Core size (nm)	Surface coating (nm)	PDI	Zeta potential (mV)
Res-PdNP-1	93 ± 4	83 ± 14	10	0.3	−26 ± 2
Res-PdNP-2	254 ± 18	53 ± 14	201	0.5	−28 ± 3
Res-PdNP-3	44 ± 1	33 ± 6	11	0.3	−31 ± 1
Res-PdNP-4	117 ± 4	24 ± 3	93	0.3	−40 ± 3

nanotechnology protocols, as described herein, have resulted in the production of four different types of Res-PdNPs (Res-PdNP-1, Res-PdNP-2, Res-PdNP-3, and Res-PdNP-4) as described in Table 1.

UV-visible spectrophotometry, dynamic light scattering (DLS), transmission electron microscopy (TEM) and inductively coupled plasma mass spectrometry (ICP-MS) were used to characterize the Res-PdNPs. UV-visible spectrophotometric analysis showed absorptions for Res and Na_2PdCl_4 with peaks at wavelengths, λ_{max} 306 nm and 420 nm, representing *trans*-Res[72–74] and Pd^{2+} ions, respectively.[75,76] UV-vis spectra of Res-PdNPs (Res-PdNP-1, 2, 3 and 4) revealed the disappearance of the 420 nm peak, confirming complete reduction of the Pd^{2+} salt with concomitant and complete transformation to Pd^0 nanoparticles as depicted in Fig. 1.

The hydrodynamic size and zeta (ζ) potential measurements of Res-PdNPs were performed using dynamic light scattering (DLS) on a Malvern instrument. Full physicochemical properties are summarized in Table 1. The zeta (ζ) potential of Res-PdNPs was <-25 mV, suggesting that Res-PdNPs have no tendency to aggregate and thus reflecting their high *in vitro* stability in solution.[77] The size distribution as evaluated by transmission electron microscopy (TEM) revealed the following average core sizes for the four different types of Res stabilized Pd nanoparticles, Res-PdNP-1, Res-PdNP-2, Res-PdNP-3 and Res-PdNP-4, to be 83 ± 14, 53 ± 14, 33 ± 6 and 24 ± 3 nm, respectively. Additionally, high resolution transmission electron microscopic (HRTEM) images revealed that Res-PdNP-1 and Res-PdNP-2 had amorphous morphologies while Res-PdNP-3 and Res-PdNP-4 exhibited crystalline lattices (Fig. 2).

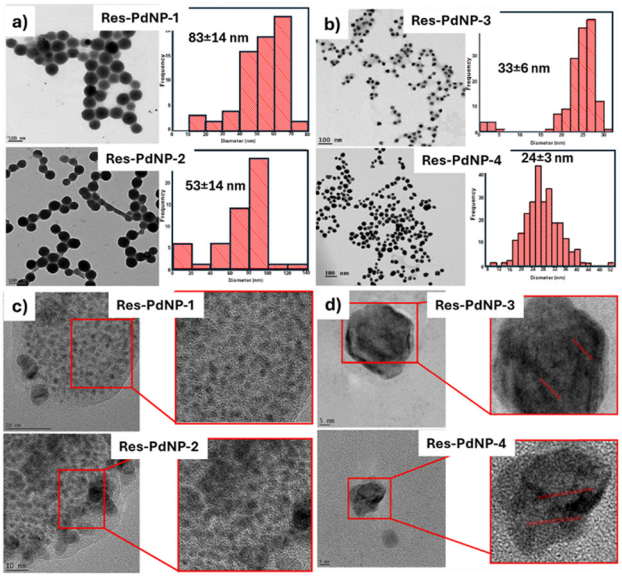

Fig. 2 Electron microscopy images with size distribution: (a) TEM images of Res-PdNP-1 and Res-PdNP-2, (b) TEM images of Res-PdNP-3 and Res-PdNP-4, (c) HRTEM images of Res-PdNP-1 and Res-PdNP-2 and (d) HRTEM images of Res-PdNP-3 and Res-PdNP-4.

Res-PdNP-1 and Res-PdNP-2 lack GA, relying solely on resveratrol for stabilization. While resveratrol can reduce metal ions and provide some stabilization, it is less effective than GA in preventing particle growth and aggregation as shown in the *in vitro* stability results (Fig. 4). This difference explains the larger sizes and reduced stability observed in Res-PdNP-1 and Res-PdNP-2. Res-PdNP-4 combines increased resveratrol with GA, resulting in a particle size of 117 nm. The larger size compared to Res-PdNP-3 is attributed to the higher resveratrol content forming a thicker corona around the nanoparticles, despite the stabilizing presence of GA.

The observed crystallization morphology for Res-PdNP-3 and Res-PdNP-4 may be attributed to the effective encapsulation by GA—thus aiding crystalline nucleation to propagate crystallization as depicted in Fig. 3.

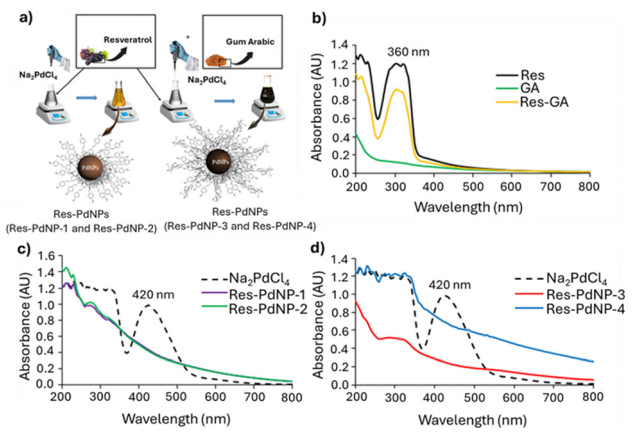

Fig. 1 UV-vis spectra of palladium nanoparticles encapsulated with resveratrol-derived phenols and polyphenols: (a) synthesis schematic, (b) free Res, GA and Res-GA mixture, (c) Res-PdNP-1 and Res-PdNP-2 and (d) Res-PdNP-3 and Res-PdNP-4.

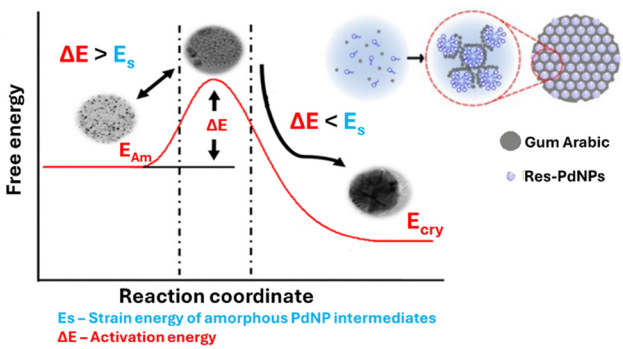

Fig. 3 Crystal growth of palladium nanoparticles influenced by GA, and a schematic illustration of the crystallization mechanism of amorphous palladium nanoparticles.

In vitro stability of Res-PdNPs

The stability of PdNPs *in vitro*, at dilutions that mimic *in vivo* biological conditions, is critical for their use in molecular imaging and therapy.[9–12,31,33,51,67,78] Therefore, we have tested the stability of Res-PdNPs (1–4) at various dilutions and in various biological fluids. Res-PdNP-1, Res-PdNP-2, Res-PdNP-3, and Res-PdNP-4 *in vitro* stability tests were conducted by dispersing Pd nanoparticles in aqueous solutions containing 1% NaCl, 0.5% cysteine, 0.2 M histidine, 0.5% HSA, and 0.5% BSA, respectively. The stability of the nanoconjugates was determined by measuring the UV absorbance over a period of 2 h, 24 h and 7 days. The persistence of the nanoparticulate composition in all biologically relevant mixtures was confirmed by a negligible/no change in UV-vis plasmon change over time. Further confirmation of the stability of different nanoparticles came from TEM experiments. Transmission electron microscopy allowed monitoring of core metallic sizes of Pd nanoparticles and revealed the retention of sizes if the particles were stable and agglomeration if the particles were unstable. For example, electron microscopic images of Res-PdNP-1 and Res-PdNP-2 showed that these nanoparticles are susceptible for agglomeration in 1% NaCl, 0.5% cysteine, 0.2 M histidine, 0.5% HSA and 0.5% BSA. However, Res-PdNP-3 and Res-PdNP-4 exhibited robustness with optimum stability in 1% NaCl, 0.5% cysteine, 0.2 M histidine, 0.5% HSA and 0.5% BSA—with no tendency to aggregate—thereby demonstrating superior *in vitro* stability in all the tested biological fluids. We infer that the additional GA encapsulant used in both Res-PdNP-3 and Res-PdNP-4 appears to confer high cohesive and adhesive electrostatic forces and thus contribute to the significantly improved and optimum stability of Res-PdNPs (Fig. 4a and b).[79] The instability of Res-PdNP-1 and Res-PdNP-2, under *in vitro* profiles, thus precluded them from inclusion in further *in vitro* and *in vivo* investigations as discussed below.

Res itself can reduce Pd^{2+} to Pd^{0} and adsorb onto the growing nanoparticle surface, imparting some negative charge and initial colloidal stability. However, as a small polyphenol it provides only limited steric protection, and ''bare'' Res–PdNPs (our Res-PdNP-1 and Res-PdNP-2) aggregated under physiological conditions as shown in Fig. 4a. In contrast, GA resulted in dramatically improved stability: GA-capped Res-PdNPs (Res-PdNP-3 and Res-PdNP-4) as shown in (Fig. 4b) exhibited robust stability at extreme dilutions, which are typical of cellular concentrations encountered under *in vivo* conditions consistent with studies that GA-coated metal NPs exhibit markedly enhanced stability in aqueous media.[80–82] This enhancement arises from GA's unique amphiphilic, high-molecular-weight structure. GA is a branched glycoprotein (a ''wattle-blossom'' architecture) whose minor hydrophobic proteinaceous chains adsorb onto the Pd surface while the long arabinogalactan polysaccharide branches extend into water.[83] The resulting polymer shell imposes strong steric hindrance; the bulky GA chains physically prevent particles from colliding and coalescing and their many ionized carboxylate groups impart a dense negative surface charge. These combined steric and electrostatic effects yield a much higher colloidal stability (and often more negative ζ-potentials) than resveratrol alone. Therefore, Res-PdNP-3 and Res-PdNP-4 (with GA) maintain their size, whereas the GA-free Res-PdNP-1 and Res-PdNP-2 samples rapidly form large aggregates. Taken together, these data indicate that GA is essential for achieving the observed enhanced stability and size control; resveratrol alone cannot provide the same long-term colloidal integrity. The above observations suggest that Res

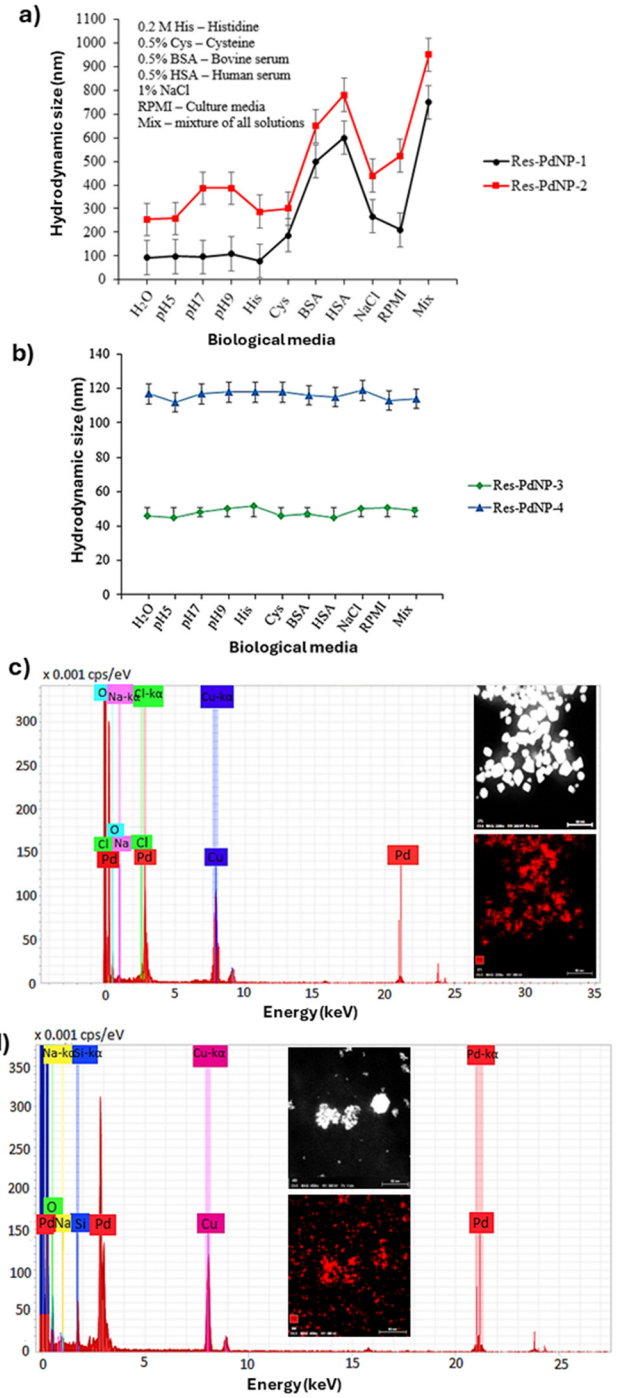

Fig. 4 *In vitro* stability and elemental analysis: (a) stability of Res-PdNP-1 and Res-PdNP-2, (b) stability of Res-PdNP-3 and Res-PdNP-4, (c) EDS of Res-PdNP-3 and (d) EDS of Res-PdNP-4 showing the presence of Pd. Res-PdNP-1 and Res-PdNP-2 not stable in BSA, HSA and mix media.

encapsulation, in combination with a biocompatible GA protein capping agent, forms a network of strongly hydrogen bonded corona around palladium nanoparticles, resulting in excellent *in vitro* and *in vivo* stability over extended periods of time in a variety of media that are biologically relevant.

Elemental analysis and quantification of Res-derived phenols and polyphenolics in Res-PdNPs

We have further analyzed Res-PdNP-3 and Res-PdNP-4 in detail using high-angle annular dark-field scanning transmission electron microscopy (HAADF-STEM) and energy-dispersive X-ray spectroscopy (EDS-STEM). The data inferred the presence of Pd metal (Fig. 4c and d). The concentration of Res-derived phenols and polyphenolic compounds encapsulated on the surfaces of Res-PdNP-3 and Res-PdNP-4 were determined to be 6 and 20 μg mL^{-1}, respectively, using liquid chromatography mass spectrometry (LC-MS/MS) with multiple reaction monitoring (MRM) on the Quantiva system (Fig. 5). Res-PdNP-4 exhibited the maximum loading of the Res corona on the nanoparticle surface. Therefore, we selected Res-PdNP-4 (referred to as Res-PdNPs) as the most ideal nanomedicine candidate for additional *in vitro* and *in vivo* studies, as discussed in the following sections.

Powder XRD analysis of Res-PdNPs

The powder X-ray diffraction (XRD) analysis of Res-PdNPs revealed peaks representing 2θ values at 40.5°, 45.9°, 68.14°, and 79.1°, respectively, corresponding to the standard Bragg reflection (111), (200), (222) and (311) planes of the face-centered cubic (fcc) lattice structure for the standard data of Pd (JCPDS no. 05–0681) (Fig. 6). The intense (111) reflection suggests preferential orientation and dominance of this facet in the Res-PdNPs.

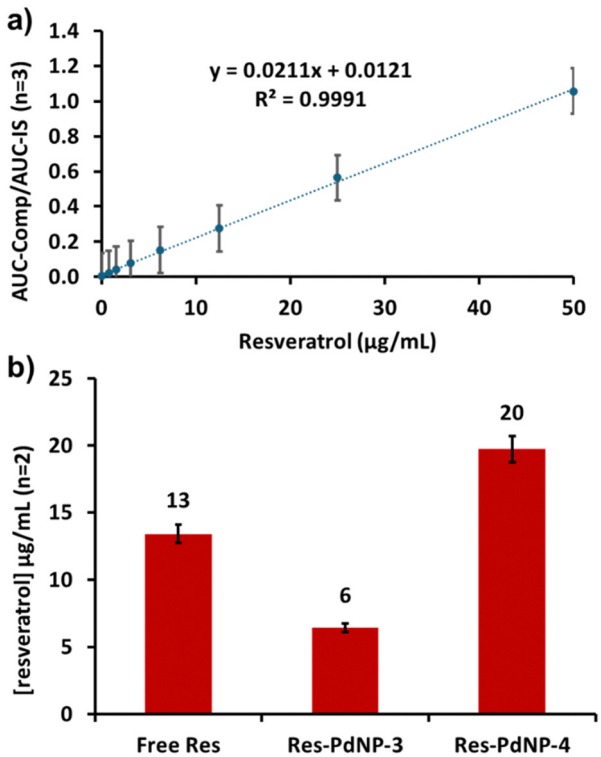

Fig. 5 LC-MS/MRM quantitation of Res: (a) Res standard curve normalized to AUC for the tolbutamide internal standard and (b) Res-PdNPs monitored by MRM to specifically quantify the resveratrol in the samples.

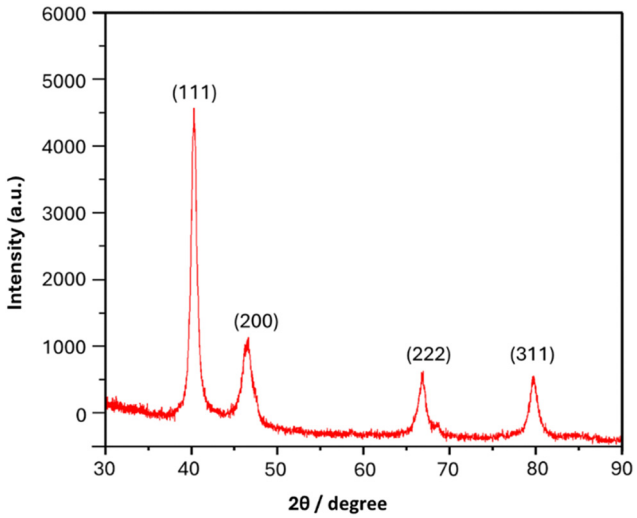

Fig. 6 Powder XRD diffraction pattern of Res-PdNPs. The presence of these distinct peaks confirms the high crystallinity and phase purity of the PdNPs.

Tumor cell specificity and receptor mediated endocytosis of Res-PdNPs

We have demonstrated, through numerous examples, that the polyphenolic structural motif of epigallocatechin gallate (EGCG) and other phytochemicals bind selectively (in the sub-nanomolar ranges) to laminin receptors that are overexpressed in prostate and several other tumors.[51] We reasoned that the chemical structure of Res, which contains a polyphenolic motif, will exhibit laminin receptor avidity, thus enabling selective targeting and accumulation of Res-PdNP-4 within prostate tumor cells that are known to over express laminin receptors. To investigate the laminin receptor specificity of Res-PdNP-4, we have conducted experimental mechanistic studies on the endocytosis pathways utilizing PC-3 prostate tumor cells derived from patient tumors. Cellular internalization of Res-PdNPs against PC-3 cells at 42 μg mL^{-1}, through dark field microscopy (CytoViva), revealed that the endocytosis of Res-PdNPs is time-dependent with optimal uptake achieved at 6 h post incubation as depicted in Fig. 7.

In order to further probe the mechanism of endocytosis, we have performed receptor blocking studies utilizing a laminin receptor antibody (MLuC5). Briefly, we treated PC-3 cells with Res-PdNPs in two different studies in the presence and absence of the MLuC5 antibody to deduce the laminin receptor mediated endocytosis of this nanomedicine agent. We were able to saturate laminin receptors over expressed in PC-3 cells by pre-incubation of these cells with the MLuC5 antibody. The hypothesis was that when laminin receptors, over expressed on prostate tumor cells (PC-3), are blocked by strong binding interactions with the MLuC5 antibody, this would result in

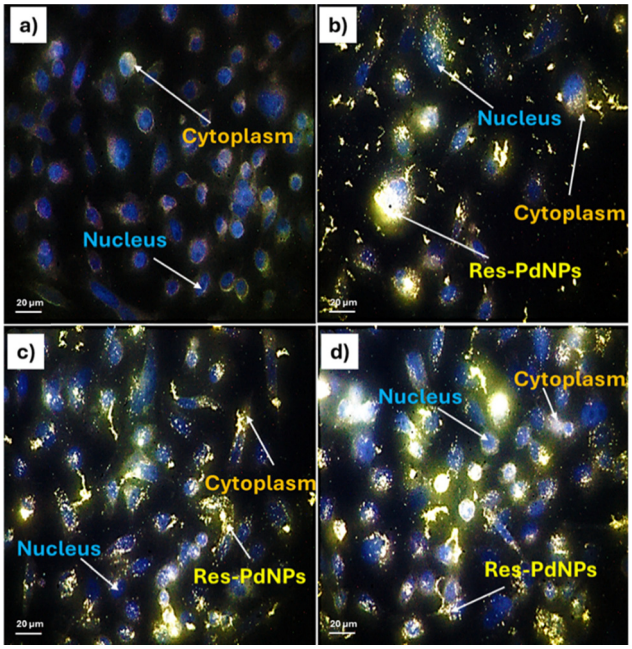

Fig. 7 Dark field CytoViva images of PC-3 cells showing cellular internalization post-treatment: (a) control (no treatment), (b) PC-3 cells incubated for 2 h, (c) PC-3 cells incubated for 6 h and (d) PC-3 cells incubated with 42 μg mL^{-1} Res-PdNPs for 24 h. Scale bar: 20 μm.

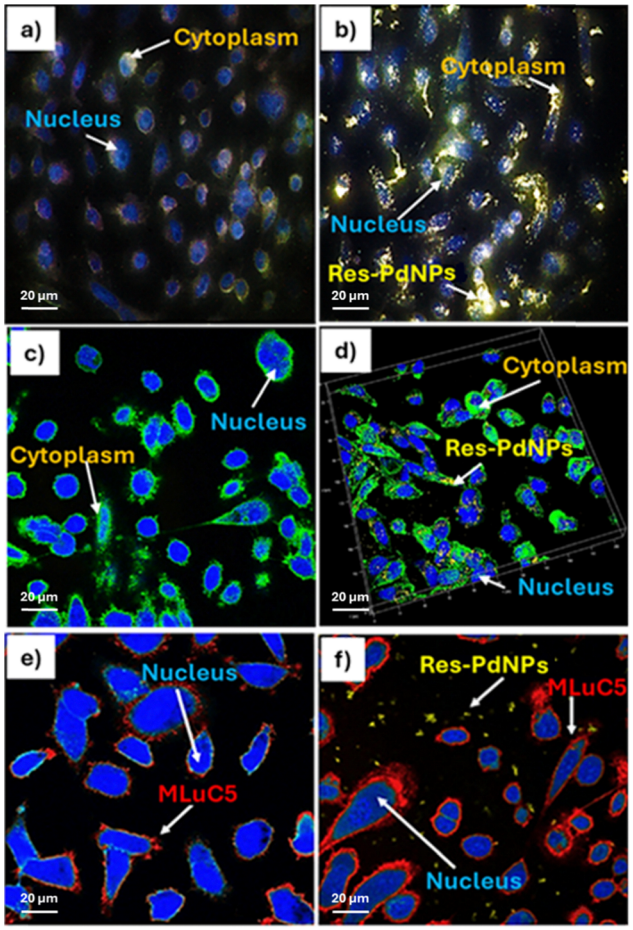

Fig. 8 Dark field CytoViva (a) and (b) and confocal (c)–(f) images of PC-3 cells. Images (a) and (c) represent dark field and confocal microscopic images before treatment with Res-PdNPs (as controls). Images (b) and (d) represent dark field and confocal microscopic images showing efficient cellular internalization post treatment with Res-PdNPs. Image (e) represents laminin receptor blocking by incubation of PC-3 cells with the laminin 67 receptor blocking antibody (MLuC5). Image (f) clearly shows the complete absence of Res-PdNPs within PC-3 cells, signifying that laminin receptor blocking stops the endocytosis of laminin receptor-specific Res-PdNPs. Nucleus (DAPI stain – blue), cytoplasm (WGA stain – green), laminin 67 receptor blocking (MLuC5 – red), and Res-PdNPs (yellow). Scale bar: 20 μm.

hindrance or complete blockage of the receptor-mediated entry of laminin-receptor specific Res-PdNPs. When the laminin receptors on PC-3 cells are not blocked with the MLuC5 antibody, we expected facile endocytosis and entry of Res-PdNPs into PC-3 cells. Our detailed results, as depicted, in Fig. 8d, unequivocally validated our hypothesis. In Fig. 8, images (a) and (c) represent dark field and confocal microscopic images respectively before treatment with Res-PdNPs (as controls). Images (b) and (d) represent dark field and confocal microscopic images showing efficient cellular internalization post treatment with Res-PdNPs. Image (e) represents laminin receptor blocking by incubation of PC-3 cells with the laminin 67 receptor blocking antibody (MLuC5). Image (f) clearly shows the complete absence of Res-PdNPs within PC-3 cells, thus signifying that laminin receptor blocking stops the endocytosis of laminin receptor-specific Res-PdNPs and that the mechanism of endocytosis of this nanomedicine agent into tumor cells is mediated through laminin receptors over-expressed by prostate and a host of human tumors.

Microscopic examination of these cells demonstrated, unequivocally, that blocking laminin receptors with the MLuC5 antibody significantly reduced Res-PdNP cellular internalization into PC-3 cells as shown in Fig. 8f. We rationalize these findings by demonstrating that pre-incubation with the MLuC5 antibody saturates laminin 67 receptor sites on PC-3 cells, thereby decreasing or eliminating the agonistic ability of Res-PdNPs to potentially bind to laminin receptors on these cells. Taken together, the results of pre- and post-blocking of laminin receptors with the MLuC5 antibody compellingly demonstrate that the resveratrol corona on Res-PdNPs is an effective tool for converting palladium nanoparticles into a laminin receptor-specific tumor targeting nanomedicine agent *via* agonistic induced endocytosis. Additionally, our cellular interrogation studies demonstrate that Res-PdNPs have the potential for use as a tumor specific molecular imaging and therapy agent in a variety of laminin receptor-positive human cancers, which include prostate, colorectal, pancreatic, certain types of breast cancers and gliomas. It may be noted that a 3D projection snapshot image, as shown in Fig. 8, captured by a Leica SP8 spectral confocal microscope revealed that the Res-PdNPs were localized inside the cytoplasm, thus further confirming the endocytosis mechanistic pathway.

Sections of PC-3 cells, post endocytosis with Res-PdNPs, were investigated through transmission electronic microscopy (TEM). Images shown in Fig. 9 clearly corroborated the data from dark field microscopy (Fig. 8) while confirming that the

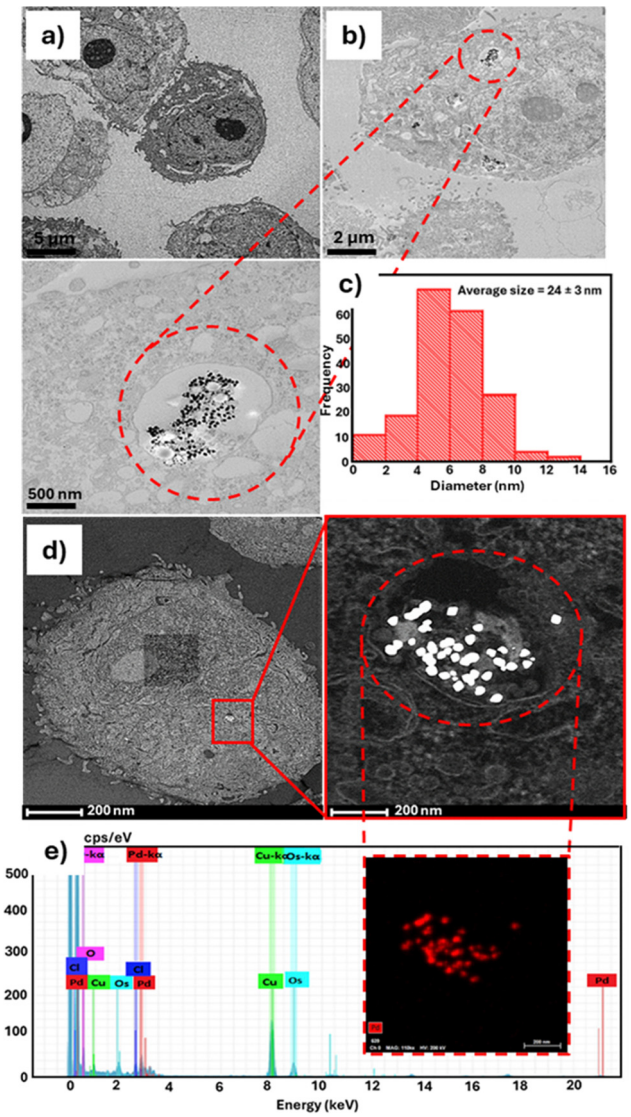

Fig. 9 TEM images indicating cellular internalization of Res-PdNPs at 6 h post treatment: (a) PC-3 control cells (no treatment), (b) PC-3 cells treated with 42 µg mL^{-1} Res-PdNPs, (c) average size distribution histogram of Res-PdNPs at 8 ± 3 nm, (d) STEM and (e) EDS mapping of PC-3 cells showing a vacuole with nanoparticles and the presence of Pd inside the prostate cancer cells.

trajectory of Res-PdNPs, to escape the endosomal pathways within the PC-3 cells, guarantees a successful delivery of payloads of Res-derived tumor specific polyphenols (and other therapeutic polyphenolic cargos) selectively into tumor cells. TEM images (Fig. 9b) also inferred that Res-PdNPs are internalized into PC-3 cells with high stability while maintaining their nanoparticulate integrity inside the tumor cells with no tendency to aggregate inside the cellular membrane. The mode of internalization was not confirmed at this point; however, TEM images confirmed an endocytic pathway based on the formation of a lysosome-like vacuole containing Res-PdNPs; these Res-PdNPs then induce autophagy and even autolysosome formation, reflecting the cell's attempt to process the foreign material. Endosomal escape or release is facilitated through the acidic endosome (pH ≈ 5.5), releasing resveratrol into the lumen or cytosol. STEM-EDS mapping performed on Res-PdNPs, internalized in the PC-3 cells, confirmed that the internalized nanoparticles are indeed non-agglomerated Res-PdNPs as shown in Fig. 9b.

Cytotoxicity of Res-PdNPs against PC-3 cells and normal human aortic endothelial cells (HAECs)

Establishing the selective cytotoxicity profile of Res-PdNPs is crucial for their translational potential as a safe and effective nanomedicine. To evaluate this, we performed colorimetric cell-viability (MTT) assay in PC-3 and HAEC cells following treatment with Res-PdNPs and reference chemotherapeutic agents (cisplatin and etoposide) at various concentrations of PdNPs (0, 2.75, 5, 11, 22 and 44 µg mL^{-1}). Fig. 10 shows the dose- and time-dependent effects of Res-PdNPs, cisplatin, and etoposide on PC-3 and HAEC cells at 48 and 72 h post treatment. In PC-3 cells (Fig. 10a and b), Res-PdNPs exhibited potent cytotoxic activity with a clear concentration-dependent decrease in cell viability, approaching the anticancer efficacy as noted for the well-known FDA approved chemotherapeutic agents cisplatin (platinum-based) and etoposide (plant-derived) at higher doses. Notably, at 44 µg mL^{-1}, Res-PdNPs reduced PC-3 cell viability significantly while preserving a less steep cytotoxicity slope compared to cisplatin and etoposide.

The relative cell viability with HAEC normal cells (Fig. 10c and d) for cisplatin and etoposide showed marked cytotoxicity with IC_{50} values for cisplatin at 2 µg mL^{-1} and etoposide at 3 µg mL^{-1} (Table 2), leading to viability reduction below 50%. In contrast, Res-PdNPs show minimal toxicity in HAEC cells with no apparent IC_{50}, indicating a strong biocompatibility profile. These findings demonstrate that Res-PdNPs offer a favorable therapeutic index, selectively inducing cytotoxicity in tumor cells while sparing normal cells. This dual profile of efficacy and safety emphasizes the promise of Res-PdNPs as a next-generation nanotherapeutic for prostate cancer treatment.

The inhibitory concentration (IC_{50}) data are summarized in Table 2. MTT results also confirmed that cisplatin and etoposide treatments were highly toxic to normal HAEC cells. However, Res-PdNPs showed minimal/no toxicity to normal cells, thus further corroborating prostate tumor cell specificity of Res-PdNPs.

Mechanism of antitumor activity of Res-PdNPs

PC-3 treated with Res-PdNPs, cisplatin, and etoposide, for 72 h post treatment at 42 µg mL^{-1}, showed dramatic morphological changes, suggesting apoptotic effects on tumor cells. This was evident due to the observation of cell shrinkage and cell debris, confirming the morphological characteristics of apoptosis (Fig. 11). HAEC cells treated with Res-PdNPs were identical to the control (no treatment), which revealed that Res-PdNPs presented no toxic effect on normal cells. However, cisplatin and etoposide, under similar conditions exhibited significant toxicity toward normal cells (Fig. 11). These data, taken together, confirmed the selective cytotoxicity of Res-PdNPs toward tumor cells.

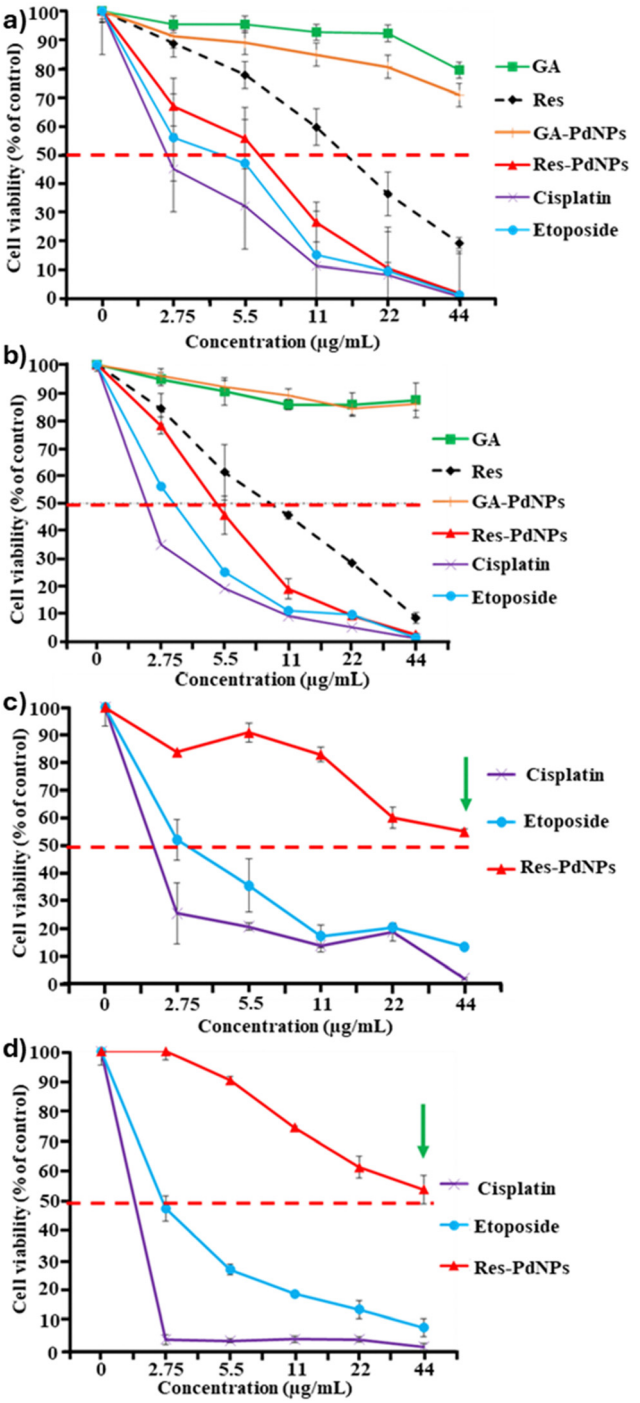

Fig. 10 Results of cell viability of the PC-3 cell line at (a) 48 h and (b) 72 h post incubation with Res-PdNPs and controls (free Res, GA, GA-PdNPs, cisplatin and etoposide), n = 4; and the HAEC cell line at (c) 48 h and (d) 72 h post incubation with Res-PdNPs and chemo-drugs (cisplatin and etoposide) reported as mean ± SEM.

Table 2 *In vitro* cellular viability studies

Sample	Cell line	IC_{50} (μg mL^{-1}) 48 h	72 h
Cisplatin	Prostate cancer (PC-3)	2	2
Etoposide		5	3
Res-PdNPs		7	5
Cisplatin	Normal human aortic endothelial cells (HAEC)	2	2
Etoposide		3	3
Res-PdNPs		N/A	N/A

IC_{50} half maximal inhibitory concentration, N/A no 50% inhibition.

Inhibition of prostate cancer cell migration

Cell migration and invasion provide a wealth of therapeutic opportunities in a variety of essential physiological and pathologic processes, most notably in the study of cancer metastasis. Cell migration studies offer a reliable paradigm in estimating the abilities of experimental drugs to inhibit cancer cell proliferation. Cancer cells possess an extraordinary propensity to move rapidly, often unstopped, towards blood vessels to procure nutrition, and this process results in rearrangements in their cytoskeleton for effective movement and invasion throughout the body for metastases and propagation in various near and distant tissues. As cancer cell migration is critical for distant metastases, therapeutic agents with capabilities of preventing migration of cancer cells might provide novel tools to fight cancer through inhibition of cell proliferation. The overarching objective of our *in vitro* investigation was to determine the effect of Res-PdNPs on the migration rate of PC-3 cells.

In our cell migration experiments, we have used the well-known scratch assay through *in vitro* wound healing of tumor cells to elucidate the inhibition of cell migration by the nanomedicine agent Res-PdNPs. Briefly, the 6-well plates were marked to monitor the region for acquiring an image. 5×10^5 cells per mL were seeded into 6-well plates and incubated for 24 h to achieve 100% confluence. By scratching through the cell monolayer with a sterile 200 μL pipette tip, a vertical wound was created aseptically. Subsequently, the debris was removed by washing the cells using the growth medium to ensure that the edges of the scratch were smoothed by repeated washing. Due care was exercised to make sure that the wounds were of similar dimensions for both the experimental and control cells to minimize any errors resulting from differences in scratch width. The cells were treated, for 24 h, with Res-PdNPs at 44 μg mL^{-1}, as shown in Fig. 12. An Olympus 1X71 Fluorescence Microscope (Shinjuku, Tokyo, Japan) was used to acquire images of untreated control PC-3 cells as well as treated cells at 0 h and 24 h post treatment and analyzed with CellSens Dimension Software 1.13 and ImageJ v1.54m Software. Results indicated that Res-PdNP treatment significantly inhibits PC-3 cell migration when compared to the images of the untreated PC-3 cells. Additionally, it is critical to note that Res-PdNP treatment of PC-3 cells decreased cell migration at concentrations well below the threshold for cytotoxicity—proving the ability of this nanomedicine agent to limit invasion of highly metastatic prostate cancer cells.

In the overall processes of cancer cell migration, invasion and adhesion are important steps in the recruitment of primary tumor cells as they spread through the circulatory and lymphatic systems. Invasion of tumor cells across the basement

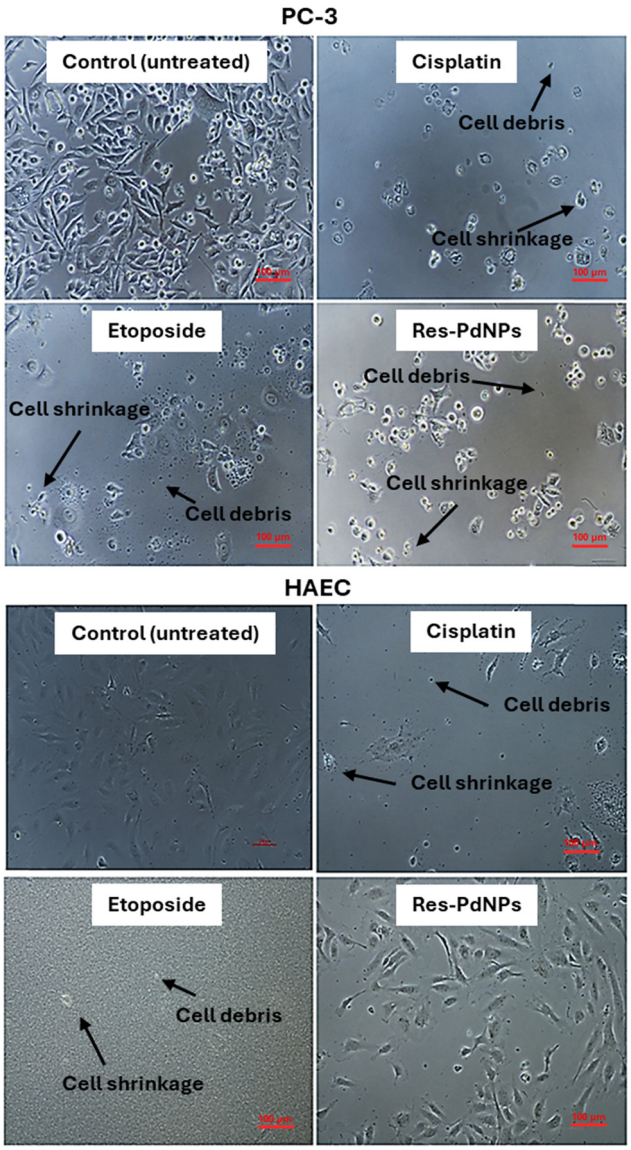

Fig. 11 Cellular morphological studies of PC-3 and HAEC cells after 72 h post incubation with cisplatin, etoposide, and Res-PdNPs for 72 h at 42 μg mL^{-1}. Res-PdNPs exhibit comparable anticancer efficacy against PC-3 as cisplatin and etoposide, attributed to the presence of cell shrinkage and cell debris, confirming the morphological characteristics of apoptosis. Cisplatin and etoposide were highly toxic to HAECs, while Res-PdNPs presented no toxicity. Scale bar: 100 μm.

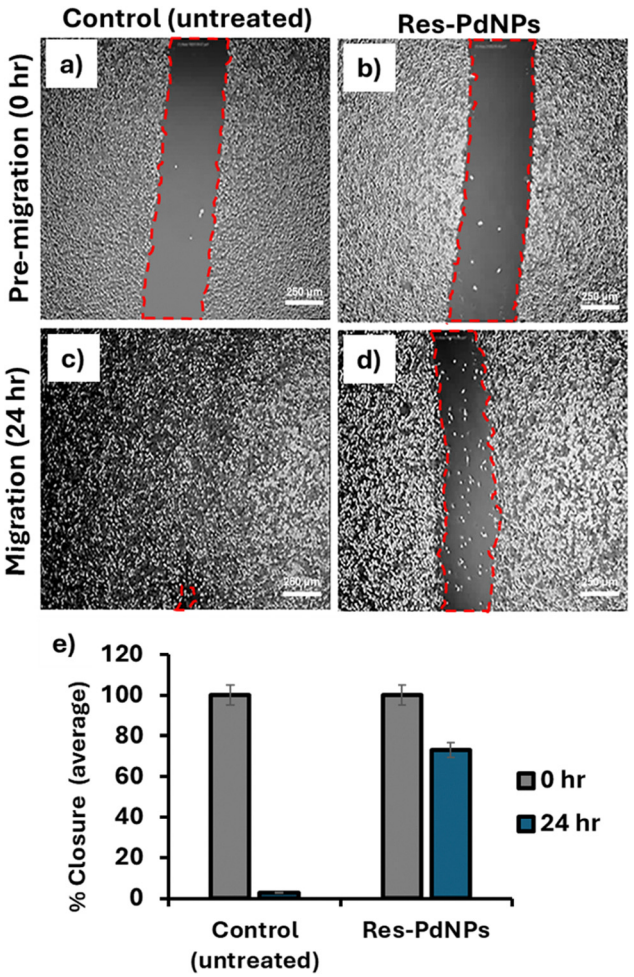

Fig. 12 Cellular migration study of prostate cancer (PC-3) cells using the scratch assay. Phase images of pre-migration at 0 h (a and b) and migration after 24 h (c) and (d), and (e) graph comparing cell migration closure (n = 3). Scale bar: 250 μm.

membranes and endothelial walls will finally result in colonization at distant organs, including bone marrow. The effective migrastatic inhibition in prostate cancer cells, as exhibited by Res-PdNPs (Fig. 12d and e), thus demonstrates the ability of this nanomedicine agent to stop cytoskeletal activity, consequently restricting cell–cell interactions with neighboring cells. The *in vitro* anti-proliferative and anti-metastases effects of Res-PdNPs, as observed in our investigations, provide realistic potential for translating this nanomedicine agent as an effective therapeutic tool for studying *in vivo* physiological processes to restrict embryonic developmental stages of tumor cells.

Evaluation of the targeting ability of Res-PdNPs toward nuclear transcription factor (NF-κB)

It is widely established that the nuclear transcription factor (NF-κB) enhances cell survival, tumor invasion, metastasis and chemoresistance during human cancer progression. Indeed, there is substantial evidence that the constitutive NF-κB expression corresponds closely to the loss of androgen receptor (AR) expression and castration-resistant characteristics in primary prostate malignancies. These findings suggest that activating NF-κB is sufficient to maintain androgen-independent (AI) prostate cancer growth *via* regulation of AR activity. As a result, the NF-κB pathway may be a therapeutic target for AI prostate cancer. When classical NF-κB signaling is activated, it promotes the expression of androgen receptor splicing variants (ARVs) in PC-3 cells and transforms androgen-sensitive PC-3 cells to become androgen-insensitive. Additionally, studies have also demonstrated that inhibiting NF-κB signaling reduces ARV expression and restores castration-resistant prostate cancer (CRPC) response to anti-androgen therapy.

These findings imply that inhibiting and decreasing NF-κB activation may be an attractive therapeutic strategy for treating

advanced stages of prostate cancer, which manifests the absence of androgen. As a result, we have investigated the potential utility of Res-PdNPs as a NF-κB targeting agent for inhibiting NF-κB p65 transcription factor activity *via* interactions with PC-3 cells. In our experiments, PC-3 cells were treated with the receptor activator of the NF-κB ligand (RANKL) only to promote NF-κB expression. This group of cells served as a positive control group while Res-PdNP treated PC-3 cells, without RANKL activation, served as a negative control group. Our experiments began with seeding PC-3 cells into 6 well plates, followed by pretreatment with Res-PdNPs (25, 50, and 100 μg mL^{-1}) for 2 h, which is followed by treatment with RANKL (25 ng mL^{-1}) or left untreated for 4 h. RANKL is a prominent activator of NF-κB pertaining to increased expression of NF-κB and further promotes metastasis in PC-3 cells through epithelial mesenchymal transition.

We used western blotting to quantify NF-κB suppressive effects of Res-PdNPs and compared them to a control set of PC-3 cells. As shown in Fig. 13, Res-PdNPs substantially inhibited RANKL-induced-NF-κB activation in the PC-3 cells, which were pretreated with the Res-PdNP nanomedicine agent. The images in Fig. 13a further revealed that the levels of NF-κB expression were much higher in the PC-3 control group—which was not pre-treated with Res-PdNPs (Fig. 13b). These findings conclusively establish that Res-PdNPs are an attractive immunomodulatory nanomedicine agent for use in the following applications as an NF-κB antagonist for inhibiting RANKL-induced-NF-κB signaling, thereby diminishing NF-κB activity that orchestrates a specific repertoire of gene expressions, inhibiting excessive tumor proliferation, and thus reducing/eliminating apoptotic resistance. These effects would result in anti-angiogenesis and inhibition of tumor cell invasion and thus effectively control/eliminate metastasis and in the overall design of new RANKL-NF-κB cancer prevention and therapeutic targets.

Additionally, it is also critical to note that drugs that inhibit NF-κB signaling in the tumor associated microenvironment (TAMs) can reprogram macrophages from the pro-tumor M2 to an anti-tumor M1 phenotype, thereby promoting regression of advanced tumors through induction of macrophage tumoricidal activity and activation of antitumor activity *via* IL-12-dependent NK cell recruitment. Given the critical role of M2 to M1 macrophage reeducation and the established role of Res-PdNPs in targeting NF-κB signaling (Fig. 14), the logical next step was to evaluate the macrophage targeting ability of Res-PdNPs, particularly its capacity to convert pro-tumor M2 to an anti-tumor M1 phenotype within TAMs. Within the tumor microenvironment, tumor-associated macrophages (TAMs) are controlled by highly dynamic cell-to-cell crosstalk between NF-κB and other signaling pathways. By modulating NF-κB activation, such crosstalk feedback controls the inflammatory response in macrophages.[84] We were intrigued to examine the effect of Res-PdNPs in targeting the tumor microenvironment because TAMs govern critical functions in promoting cancer cell metastatic cascades through modifications in tumor proliferation, migration, invasion, angiogenesis, and immunosuppression. The intrinsic connection between NF-κB signaling

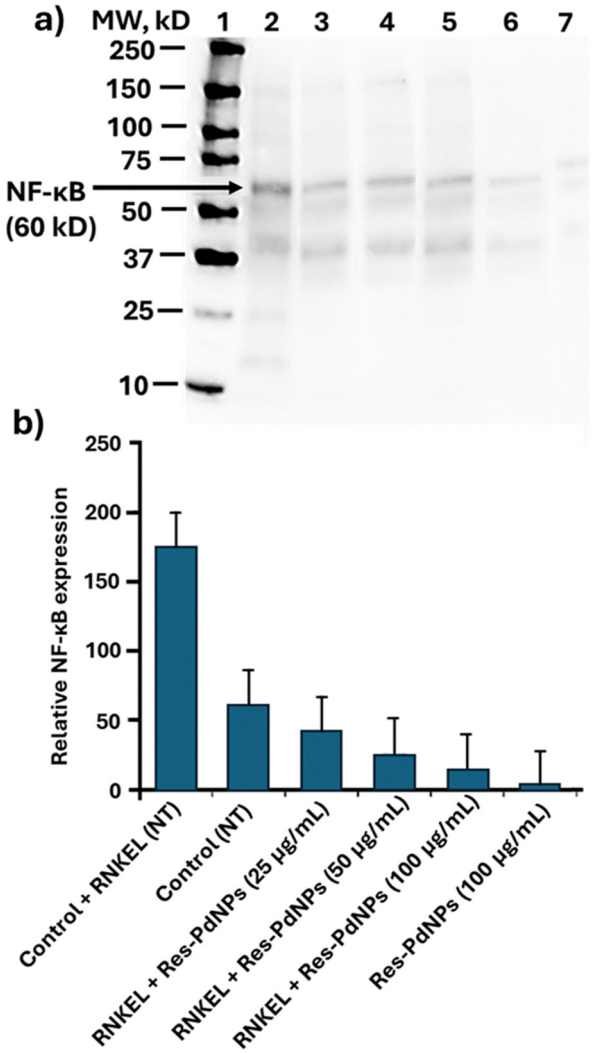

Fig. 13 (a) Western blot analysis. Lanes 1: Std protein ladder; 2: control + RANKL (NT); 3: control (NT); 4: RANKL + Res-PdNPs (25 μg mL^{-1}); 5: RANKL + Res-PdNPs (50 μg mL^{-1}); 6: RANKL + Res-PdNPs (100 μg mL^{-1}) and (b) relative NF-κB expression level.

and macrophage activation has been explored through the ability of Res-PdNPs to elevate anti-tumor cytokine M1 markers (IL-1β, TNF-α, IL-6, and IL-12), which are linked to M1 macrophage polarization, while simultaneously reducing pro-tumor cytokine M2 markers (TGF-β1 and IL-10), which are characteristic of M2 macrophage polarization.[62] Notably, IL-6 can exhibit dual functions depending on the context, but it is generally classified as a pro-inflammatory cytokine in most acute inflammatory responses (Fig. 14). These data are corroborated by Sungu *et al.*[85] work, they showed PdNPs (25 nm) induced M1 polarization of macrophages. Additionally, human THP-1 monocytes treated with PdNPs drastically increased secretion levels of M1 cytokines (IL-1β, TNF-α, and IL-6) in exosomes than that in controls.[86]

This results in the production of pro-inflammatory cytokines, which activate the tumor NF-κB pathway of tumor cells and tumor-infiltrating cells such as macrophages and myeloid-

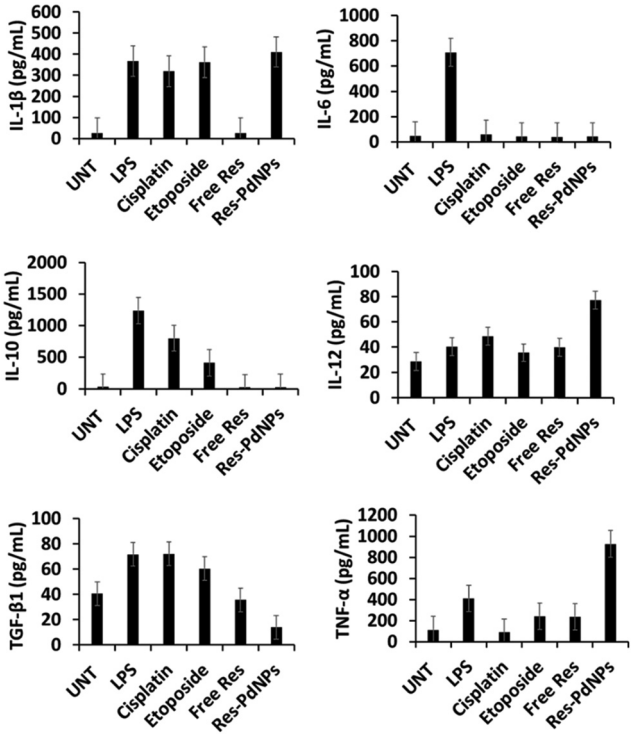

Fig. 14 Res-PdNP induced polarization of M1 macrophage anti-tumor cytokines (IL-1β, TNF-α, IL-6, IL-12) with concomitant reduction in the levels of pro-tumor cytokines (TGF-β1 and IL-10). $P < 0.05$ *vs.* the LPS group.

derived suppressor cells (MDSCs), ultimately creating a tumor-permissive environment conductive to growth and metastasis. In the following sections, we will discuss our results on the ability of Res-PdNPs to target macrophages and how this capability can be used to tailor macrophage machinery into the design of a new immunomodulatory prostate cancer therapeutic agent.

Evaluation of the targeting ability of Res-PdNPs toward tumor-infiltrating macrophages

Macrophages are non-neoplastic cells that exhibit either pro-tumor or anti-tumor phenotypes, depending on their anatomical origin and physiological function. Within the macrophage phenotype spectrum, classically activated macrophages (known to as M1 phenotype) are generated by T-helper 1 (Th-1) cytokines, whereas alternatively activated macrophages (referred to as M2 phenotype) are induced by Th-2 cytokines.[87,88] TAMs demonstrate phagocytic activity against pathogens and tumoricidal activity *via* induction of anti-tumor cell recruitment of IL-12-dependent natural killer cells (NK). In contrast, human proliferating tumors have a polarized M2 phenotype that coordinates tumor metastasis and eventually contributes to multi-therapeutic drug resistance.[89] Clinical data suggest that macrophage infiltrations have a role in the archetypical carcinogenesis of prostate cancer, which is frequently associated with metastatic prostate cancer. Indeed, castrated tumors include a high proportion of pro-tumorigenic M2 macrophages, resulting in the greatest immunosuppressive effects.

It is therefore imperative to explore the possibility of developing drugs capable of targeting and inhibiting NF-κB signaling in TAMs aimed at converting macrophages from pro-tumor M2 to an anti-tumor M1 phenotypic state.[90] This approach represents a potential therapeutic intervention against a myriad of diseases. Due to the ability of Res-PdNPs to effectively target NF-κB signaling, we sought to investigate the potential therapeutic strategy for its role in reprogramming pro-tumor M2 to the anti-tumor M1 macrophage phenotype. Our experiments for evaluating Res-PdNP-4 capacity to target tumor-infiltrating macrophages included pre-treatment of RAW 264.7 macrophages with Res-PdNPs. As shown in Fig. 15b, the Res-PdNPs exhibited excellent affinity and proclivity to internalize within RAW 264.7 macrophages *via* phagocytosis. Indeed, after 60 min, macrophages absorbed considerable amounts of Res-PdNPs. These investigations established selective avidity of Res-PdNPs for pro-tumor M2 macrophages.

To determine whether the Res-PdNP nanomedicine agent can reprogram pro-tumor M2 macrophages into the therapeutically desirable anti-tumor M1 phenotype, we co-cultured Res-PdNPs-pretreated RAW 264.7 macrophages with PC-3 cells and then compared tumor proliferation between this group and the control PC-3 cells, which were treated directly with naïve macrophages. From these experiments, we discovered that macrophages, transfected with Res-PdNPs, expressed genes in a manner consistent with the anti-tumor M1 phenotype. This observation is consistent with the highly effective anti-tumor activity of Res-PdNPs as evidenced through the large reduction in tumor cell growth, as depicted in Fig. 15d. However, the coculture of PC-3 cells with naïve macrophages failed to inhibit PC-3 cell growth (Fig. 15c). Taken together, these findings infer

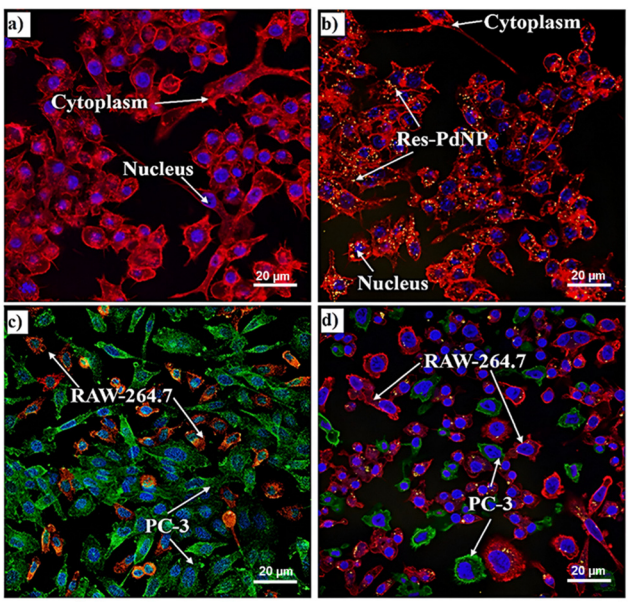

Fig. 15 Co-culture studies: (a) RAW 264.7 macrophage (untreated), (b) pre-treated RAW 264.7 cells (red) with Res-PdNPs (yellow), (c) untreated RAW 264.7 cells (red) + PC-3 (green), and (d) Res-PdNP pre-treated RAW 264.7 cells (red, Res-PdNP – yellow) + PC-3 cells (green).

the powerful immunomodulatory therapeutic features of Res-PdNPs and their ability to serve as a new cancer therapy agent with their therapeutic action mediated through the promotion of the anti-tumor M1 phenotype *in vivo*.

The ability of Res-PdNPs to target the NF-κB signalling pathway and its efficacy in the induction of polarization of macrophages to the anti-tumor phenotype by inhibiting NF-κB phosphorylation, with consequent promotion of anti-tumor cytokines, such as IL-12, as discussed above—individually and collectively—highlight the immunomodulatory features of this new nanomedicine agent. Therefore, *in vivo* therapeutic efficacy studies of Res-PdNPs in tumor models were clearly an obvious next step to evaluate whether the various immunomodulatory parameters, as observed *in vitro*, would be translated under the more complex *in vivo* tumor profiles in tumor bearing mice. We have therefore undertaken detailed therapeutic efficacy studies of Res-PdNPs in prostate tumor bearing SCID mice as discussed below.

Therapeutic efficacy of Res-PdNPs in treating prostate tumor

Severely compromised immunodeficient (SCID) mice bearing a flank model of human prostate cancer, derived from a subcutaneous implant of 10 million PC-3 cells, were used for the therapeutic efficacy and pharmacokinetic studies. As discussed in the experimental section, unilateral solid tumors were allowed to grow for three weeks, and animals were randomized (denoted day 0) into control and treatment groups (n = 7) with no significant differences in tumor volume. *In vivo* dosing involved administering on day 0 three doses of Res-PdNPs (0.25 mg kg^{-1} bw and 1.0 mg kg^{-1} bw—in 100 μL Dulbecco's PBS) intravenously through the tail vein, while the control SCID mice received only 100 μL Dulbecco's PBS/saline. This treatment regimen was performed twice per week. Tumors were then measured twice each week until the end of the study (day 35). Fig. 16a shows results from the Res-PdNP-treated human prostate cancer bearing SCID mice. Within two weeks (day 14), tumor growth in the treated animals started slowing down with respect to the control animals. On day 21, post administration of Res-PdNPs (0.25 mg kg^{-1} bw and 1.0 mg kg^{-1} bw), tumor volumes were two-fold lower ($p < 0.005$) for treated animals as compared to the control group. Five weeks post administration of Res-PdNPs (1 mg kg^{-1} bw), tumor volumes of the control animals were fully five-fold greater with respect to those of the Res-PdNPs-treated group ($p < 0.0001$; 0.37 ± 0.05 *vs.* 0.06 ± 0.02 cm^3)—suggesting >85% reduction in the overall tumor volume for the treated group. This significant therapeutic effect was maintained throughout the 35 day long study. Tumors harvested from the treatment group consisted largely of necrotic tissue, indicating extensive death of tumor cells.

The unequivocal therapeutic efficacy data, as summarized above, bear strong relevance for clinical translation in treating human patients because all the two therapeutic doses (0.25 mg kg^{-1} bw and 1.0 mg kg^{-1} bw) are well tolerated in animals as shown in Fig. 16b. The body weights throughout the treatment period, at all two doses, were very similar to the control, untreated group, suggesting excellent tolerance of Res-PdNPs throughout the treatment period.

The *in vivo* therapeutic efficacy data, as described above, may be rationalized in terms of the synergistic effects of the ability of Pd nanoparticles to deliver optimum doses of the therapeutic resveratrol cargo into tumor cells in conjunction with the inherent anti-angiogenesis and immunomodulatory characteristics of Pd nanoparticles. The corona created by Res on the Pd nanoparticulate surface is dislodged efficiently within tumor cells, thus resulting in the enhancement of bioavailability of the therapeutic phytochemical. PdNPs exhibit remarkable photothermal properties that augment their role as drug carriers. PdNPs have a broad and strong optical absorption extending into the near-infrared (NIR) region, which is optimal for deep tissue penetration. They efficiently convert NIR light into heat, enabling photothermal therapy (PTT). Notably, Pd nanostructures (such as ultrathin Pd nanosheets and porous PdNPs) have demonstrated photothermal conversion efficiencies exceeding 90% upon 808 nm laser irradiation.[91]

This is better than the best reported gold nanostructures, and critically, palladium maintains excellent photothermal stability. Therefore, a PdNP-phytochemical conjugate could thus serve as a dual-mode therapy: delivering a phytochemical

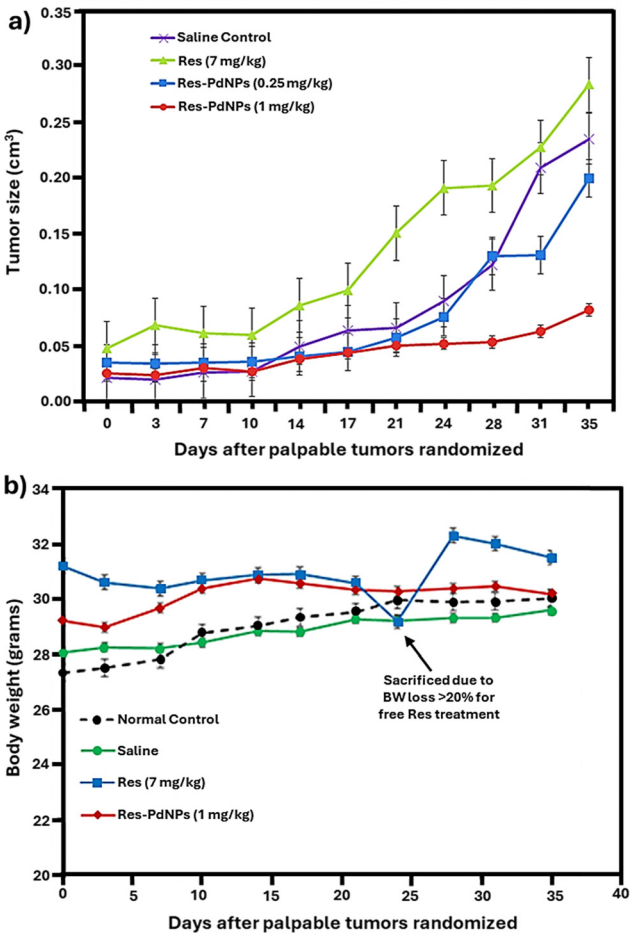

Fig. 16 Therapeutic efficacy studies: (a) prostate tumor-bearing SCID male mice treated by intravenous injection twice a week with Res-PdNPs, Res and saline and (b) average body weight of the SCID male mice during the study.

drug and concurrently enabling PTT upon NIR laser irradiation. Even though our current manuscript does not extensively delve into photothermal experiments, we highlight this attribute to underscore the novelty and theranostic potential of the PdNP system. The ability to induce localized hyperthermia can synergistically enhance the anticancer effects of the released phytochemicals (through improved drug uptake and heat-induced cancer cell apoptosis). This multi-functional capacity (chemotherapeutic + photothermal) of PdNPs is a clear advantage over traditional AuNP carriers, adding a novel therapeutic dimension to our platform.

The hematology data indicated that systemic Res-PdNP treatment did not perturb normal blood parameters. White blood cell (WBC) counts in the Res-PdNP group ($2.2 \pm 1.1 \times 10^3\ \mu L^{-1}$) were well within the normal physiological range and statistically indistinguishable from the untreated control ($1.6 \pm 0.5 \times 10^3\ \mu L^{-1}$, $p > 0.05$). By comparison, the saline and free resveratrol groups showed higher WBC means ($3.7 \pm 2.0 \times 10^3\ \mu L^{-1}$ and $3.5 \pm 1.4 \times 10^3\ \mu L^{-1}$, respectively), although these elevations did not reflect pathological leukocytosis and were also not statistically significant (Fig. 17). Platelet levels likewise remained unaltered by Res-PdNPs: the Res-PdNP group exhibited an average of $697.5 \pm 174.6 \times 10^3\ \mu L^{-1}$ platelets, essentially the same as control ($657.5 \pm 212.3 \times 10^3\ \mu L^{-1}$, $p > 0.05$). Only the saline group exhibited a modest but significant platelet elevation ($\sim 900 \times 10^3\ \mu L^{-1}$, $p < 0.01$ *vs.* control), perhaps reflecting a minor stress response to fluid administration. Crucially, Res-PdNPs did not induce thrombocytosis or any statistically significant change in platelet count (ns *vs.* control).

Similarly, red blood cell (RBC) counts, hemoglobin (Hb) concentrations, and lymphocyte counts in the Res-PdNP cohort were indistinguishable from those in control and free-Res groups (all $p > 0.05$). All measured values for Res-PdNP-treated animals fell squarely within the normal ranges for healthy subjects, with no indication of anemia, hemolysis, or lymphocyte depletion. Res-PdNPs showed complete hematological neutrality with none of the key parameters (WBC, RBC, Hb, lymphocytes, and platelets) deviating significantly from normal. These data strongly support the conclusion that Res-PdNPs do not elicit hematotoxicity. Similarly, resveratrol-loaded polymeric nanoparticles were non-hepatotoxic.[92] Work conducted by Wang *et al.*[93] reported that Pd nanoplate-treated mice showed no abnormal changes in blood tests, including WBC, platelets, RBC, and Hb compared to controls. Pd-based nanomaterials have demonstrated good biocompatibility and no overt adverse effects on blood or major organs in rodent models.[94] Each of these *in vivo* studies consistently demonstrated that resveratrol-loaded and palladium-based nanoparticles were well tolerated in rodent models, exhibiting no significant hematological toxicity, as evidenced by normal levels of WBCs, RBCs, and platelets. Moreover, these formulations achieved favorable therapeutic outcomes, including notable tumor regression. Collectively, the findings validate that Res-PdNPs are not only safe but also therapeutically comparable or superior to free resveratrol. Notably, Res-PdNPs showed a hematological safety profile at least equivalent to free resveratrol and

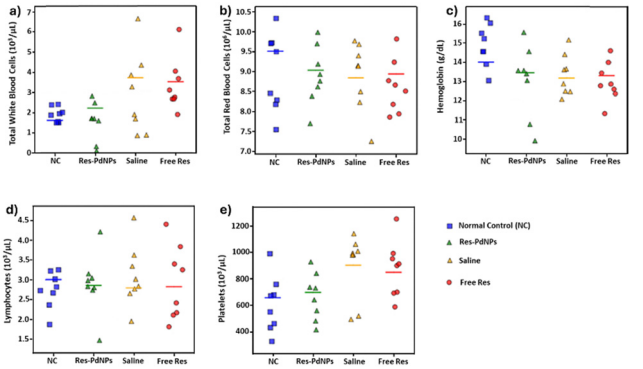

Fig. 17 Hematological evaluation of the *in vivo* safety profile of Res-PdNPs in comparison to control and other treatment groups. (a)–(e) Hematological parameters measured include (a) white blood cells (WBCs), (b) red blood cells (RBCs), (c) hemoglobin, (d) lymphocytes, and (e) platelet count. Treatment groups include normal control (no treatment) (blue squares), Res-PdNPs (green triangles), saline (yellow triangles), and free resveratrol (red circles). Horizontal lines denote mean ± SEM for each group (n = 6).

significantly more favorable than the stress-associated hematological changes observed in the saline control group. These results affirm that the palladium nanocarrier does not induce additional systemic or blood-related toxicity, underscoring its potential as a safe and effective drug delivery platform.

Immunohistochemistry of tumor xenografts

We have further measured the mean microvessel density (MVD) in our efforts to evaluate neovascularization *in vivo* through CD31 staining. Quantification was performed using ImageJ v1.54m Immunohistochemistry (IHC) Image Analysis software. Res-PdNP treatment revealed a substantial decrease in the

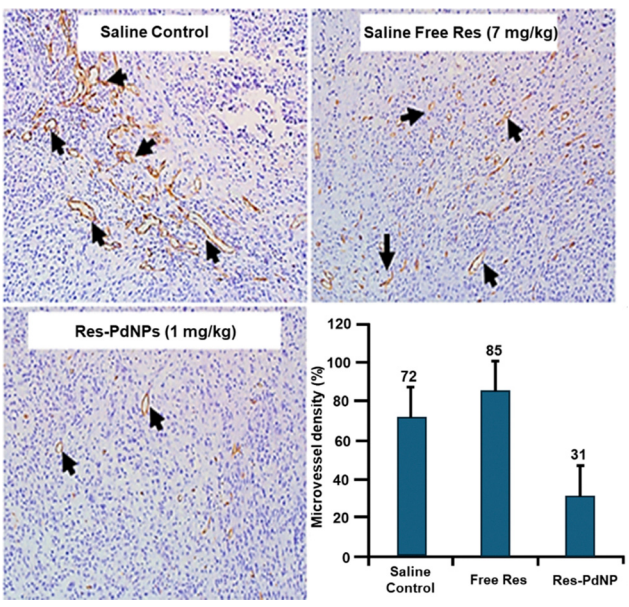

Fig. 18 Immunohistochemical CD31 staining of tumor tissues to evaluate blood vessels. Twelve fields from each xenograft were analyzed to determine the average number of vessels per field (microvessel density = MVD). n = 3; mean ± STEM.

number of MVD at 35 ± 5 vessels per mm^2 compared to the saline control as well as in animals treated with free Res, which showed 72 ± 3 and 85 ± 5 vessels per mm^2, respectively (Fig. 18). The observed MVD data corroborates the compelling therapeutic efficacy results *in vivo*, as discussed above. These observations suggest that Res-PdNPs can effectively retard the growth of tumors as compared to the saline and free Res treated groups. Analysis of tissue CD31 biomarkers showed that the Res-PdNPs inhibited angiogenesis in tumor tissue. The *in vivo* therapeutic efficacy data and the corroborating mechanisms attest to the validation of our hypothesis that the nature of the bonding interaction of resveratrol (Res) on the surface of Pd nanoparticles is optimal for the selective and efficient delivery of Res as well as the Pd nanoparticles into tumor cells/tumor tissue. The anomalous electronic configuration of Pd, exhibiting the [Kr] $4d^{10}$ configuration, suggests tremendous scope in developing the tumor-avid corona on the surface of palladium nanoparticles for augmenting bioavailability and thereby translating into optimum therapeutic efficacies.

Conclusions

The redox potential of Res is ideal in the development of Res functionalized PdNPs. Additional stabilization for *in vitro* and *in vivo* stability, as well as enhancing the Res corona, is afforded by the FDA approved gum Arabic plant protein. The *in vitro* cellular internalization investigations inferred that Res-PdNP-4 is selective to the laminin receptors overexpressed in PC-3 cells. MTT assays have confirmed that the Res cargo, in conjunction with the inherent anti-tumor effects of the Pd metal, makes Res-PdNP-4 a new generation of immunomodulatory nanotherapeutic agent for treating prostate and various other laminin receptor positive tumors. The selective targeting of Res-PdNPs toward macrophages has been corroborated by the excellent therapeutic efficacy results in prostate tumor bearing mice. These results, taken together, provide a niche in developing future immunotherapeutic agents for treating cancer through the green nanotechnology of palladium. Overall, the anomalous electronic configuration of palladium, as compared to gold and other metals, might hold a realistic promise in the design and development of sophisticated PdNP-based cancer diagnostic and therapy agents with attractive implications in oncology. The relative nontoxic nature of Res-PdNPs, as compared to the well-known cisplatin and etoposide drugs, which are highly toxic to normal cells, makes a compelling case for further developing this class of PdNP-based nanoceuticals for cancer therapy for their ultimate applications in treating human patients.

Author contributions

Data curation, formal analysis, investigation, writing – original draft: Velaphi C. Thipe; writing – reviewing and editing: Alice Raphael Karikachery, Kavita Katti; and conceptualization, funding acquisition, writing – reviewing and editing: Kattesh V. Katti.

Data availability

The datasets generated and/or analyzed during the current study are available in the article. Additional raw data and any further details supporting the conclusions of this study are available from the corresponding author upon reasonable request.

Conflicts of interest

There are no conflicts to declare.

Acknowledgements

The authors thank the South Africa National Research Foundation for financial support through a Fulbright Scholarship to Velaphi Thipe. We also thank the University of Missouri, Institute of Green Nanotechnology, where this research was conducted for logistical support. The University of Missouri Electron Microscopy Core Facility is gratefully acknowledged. This work has been supported by grants from Fulbright Foreign Student Program Grant No. 15150089, National Research Foundation of South Africa – Nanobiotechnology for cancer therapy S&F – Doctoral Abroad Grants Grant No. 98141, and University of Missouri Electron Microscopy Core (EMC) & the Office of Research – Excellence in Electron Microscopy Awards. Partial funding was obtained through the Institute of Green Nanotechnology, within the Department of Radiology, University of Missouri Medical School, University of Missouri, Columbia, Missouri, USA.

References

1 C. Andreou, S. Pal, L. Rotter, J. Yang and M. Kircher, Molecular Imaging in Nanotechnology and Theranostics, *Mol. Imaging Biol.*, 2017, **19**, DOI: 10.1007/s11307-017-1056-z.
2 A. Owen, D. Moscatelli, J. F. Lovell, K. V. Katti and M. Mazza, The application of nanotechnology in medicine: treatment and diagnostics, *Nanomedicine*, 2014, **9**, 1291–1294, DOI: 10.2217/nnm.14.93.
3 D. R. Mccormack, K. Bhattacharyya, R. Kannan, D. Ph, K. Katti and D. Ph, Enhanced Photoacoustic Detection of Melanoma Cells Using Gold Nanoparticles, *Lasers Surg. Med.*, 2011, **338**, 333–338, DOI: 10.1002/lsm.21060.
4 Y. Liu, J. Li, M. Chen, X. Chen and N. Zheng, Palladium-based nanomaterials for cancer imaging and therapy, *Theranostics*, 2020, **10**(22), 10057–10077, DOI: 10.7150/thno.45990.
5 J. Liu, T. Lécuyer and J. Seguin, *et al.*, Imaging and therapeutic applications of persistent luminescence nanomaterials, *Adv. Drug Delivery Rev.*, 2019, **138**, 193–210, DOI: 10.1016/j.addr.2018.10.015.
6 V. K. Chaturvedi, A. Singh, V. K. Singh and M. P. Singh, Cancer Nanotechnology: A New Revolution for Cancer Diagnosis and Therapy, *Curr. Drug Metab.*, 2018, **20**(6), 416–429, DOI: 10.2174/1389200219666180918111528.

7 C. Wang, W. Fan, Z. Zhang, Y. Wen, L. Xiong and X. Chen, Advanced Nanotechnology Leading the Way to Multimodal Imaging-Guided Precision Surgical Therapy, *Adv. Mater.*, 2019, **31**(49), 1–32, DOI: **10.1002/adma.201904329**.

8 E. Boote, G. Fent and V. Kattumuri, *et al.*, Gold Nanoparticle Contrast in a Phantom and Juvenile Swine: Models for Molecular Imaging of Human Organs using X-ray Computed Tomography, *Acad. Radiol.*, 2010, **17**(4), 410–417, DOI: **10.1016/j.acra.2010.01.006**.

9 M. Khoobchandani, K. K. Katti and A. R. Karikachery, *et al.*, New Approaches in Breast Cancer Therapy Through Green Nanotechnology and Nano-Ayurvedic Medicine - Pre-Clinical and Pilot Human Clinical Investigations, *Int. J. Nanomed.*, 2020, **15**, 181–197, DOI: **10.2147/IJN.S219042**.

10 A. Y. Al-Yasiri, M. Khoobchandani and C. S. Cutler, *et al.*, Mangiferin functionalized radioactive gold nanoparticles (MGF-198AuNPs) in prostate tumor therapy: Green nanotechnology for production: *In vivo* tumor retention and evaluation of therapeutic efficacy, *Dalton Trans.*, 2017, **46**(42), 14561–14571, DOI: **10.1039/c7dt00383h**.

11 T. M. Sakr, M. Korany and K. V. Katti, Journal of Drug Delivery Science and Technology Selenium nanomaterials in biomedicine—An overview of new opportunities in nanomedicine of selenium, *J. Drug Delivery Sci. Technol.*, 2018, **46**(February), 223–233, DOI: **10.1016/j.jddst.2018.05.023**.

12 A. M. Gamal-Eldeen, D. Moustafa and S. M. El-Daly, *et al.*, Gum Arabic-encapsulated gold nanoparticles for a non-invasive photothermal ablation of lung tumor in mice, *Biomed. Pharmacother.*, 2017, **89**, 1045–1054, DOI: **10.1016/j.biopha.2017.03.006**.

13 W. Pasanphan, T. Rattanawongwiboon, S. Choofong, O. Güven and K. K. Katti, Irradiated chitosan nanoparticle as a water-based antioxidant and reducing agent for a green synthesis of gold nanoplatforms, *Radiat. Phys. Chem.*, 2015, **106**, 360–370, DOI: **10.1016/j.radphyschem.2014.08.023**.

14 T. Tangthong, T. Piroonpan and V. C. Thipe, *et al.*, Water-Soluble Chitosan Conjugated DOTA-Bombesin Peptide Capped Gold Nanoparticles as a Targeted Therapeutic Agent for Prostate Cancer, *Nanotechnol., Sci. Appl.*, 2021, **14**, 69–89, DOI: **10.2147/NSA.S301942**.

15 M. Khoobchandani, A. Khan and K. K. Katti, *et al.*, Green nanotechnology of MGF-AuNPs for immunomodulatory intervention in prostate cancer therapy, *Sci. Rep.*, 2021, **11**(1), 16797, DOI: **10.1038/s41598-021-96224-8**.

16 K. K. Katti, V. Kattumuri, S. Bhaskaran, K. V. Katti and R. Kannan, Facile and general method for synthesis of sugar-coated gold nanoparticles, *Int. J. Green Nanotechnol. Biomed.*, 2009, **1**(1), B53–B59, DOI: **10.1080/19430850902983848**.

17 R. Shukla, S. K. Nune and N. Chanda, *et al.*, Soybeans as a Phytochemical Reservoir for the Production and Stabilization of Biocompatible Gold Nanoparticles, *Small*, 2008, **4**(9), 1425–1436, DOI: **10.1002/smll.200800525**.

18 N. Chanda, R. Shukla, K. V. Katti and R. Kannan, Gastrin releasing protein receptor specific gold nanorods: breast and prostate tumor avid nanovectors for molecular imaging, *Nano Lett.*, 2009, **9**(5), 1798–1805, DOI: **10.1021/nl8037147**.

19 R. Kannan, V. Rahing and C. Cutler, *et al.*, Nanocompatible Chemistry toward Fabrication of Target-Specific Gold Nanoparticles, *J. Am. Chem. Soc.*, 2006, **128**(35), 11342–11343, DOI: **10.1021/ja063280c**.

20 A. N. Geraldes, A. Alves and J. Leal, *et al.*, Green Nanotechnology from Plant Extracts: Synthesis and Characterization of Gold Nanoparticles, *Adv. Nanopart.*, 2016, 176–185.

21 S. K. Nune, N. Chanda and R. Shukla, *et al.*, Green nanotechnology from tea: phytochemicals in tea as building blocks for production of biocompatible gold nanoparticles, *J. Mater. Chem.*, 2009, **19**(19), 2912–2920, DOI: **10.1039/B822015H**.

22 V. Kattumuri, K. K. Katti and S. Bhaskaran, *et al.*, Gum arabic as a phytochemical construct for the stabilization of gold nanoparticles: *In vivo* pharmacokinetics and X-ray-contrast-imaging studies, *Small*, 2007, **3**(2), 333–341, DOI: **10.1002/smll.200600427**.

23 K. V. Katti, Realms of green nanotechnology, *Int. J. Green Nanotechnol.*, 2013, **5**(1), 1, DOI: **10.1177/1943089213509648**.

24 K. V. Katti, M. Khoobchandani and V. C. Thipe, *et al.*, Prostate tumor therapy advances in nuclear medicine: green nanotechnology toward the design of tumor specific radioactive gold nanoparticles, *J. Radioanal. Nucl. Chem.*, 2018, **318**(3), 1737–1747, DOI: **10.1007/s10967-018-6320-4**.

25 M. Khoobchandani, K. K. Katti, A. R. Karikachery, V. C. Thipe, P. L. R. Bloebaum and K. V. Katti, in *Biotechnology Products in Everyday Life*, ed. M. Khoobchandani and A. Saxena, Springer, Cham, 2019, pp. 37–52, DOI: **10.1007/978-3-319-92399-4_3**.

26 R. Shukla, N. Chanda and A. Zambre, *et al.*, Laminin receptor specific therapeutic gold nanoparticles (198AuNP-EGCg) show efficacy in treating prostate cancer, *Proc. Natl. Acad. Sci. U. S. A.*, 2012, **109**(31), 12426–12431, DOI: **10.1073/pnas.1121174109**.

27 N. Chanda, V. Kattumuri and R. Shukla, *et al.*, Bombesin functionalized gold nanoparticles show *in vitro* and *in vivo* cancer receptor specificity, *Proc. Natl. Acad. Sci. U. S. A.*, 2010, **107**(19), 8760–8765, DOI: **10.1073/pnas.1002143107**.

28 P. Jawaid, M. U. Rehman and Q. L. Zhao, *et al.*, Small size gold nanoparticles enhance apoptosis-induced by cold atmospheric plasma via depletion of intracellular GSH and modification of oxidative stress, *Cell Death Discov.*, 2020, **6**(1), 83, DOI: **10.1038/s41420-020-00314-x**.

29 N. Chanda, R. Shukla, K. V. Katti and R. Kannan, Gastrin Releasing Protein Receptor Specific Gold Nanorods: Breast and Prostate Tumor Avid Nanovectors for Molecular Imaging, *Nano Lett.*, 2009, **9**, 1798–1805, DOI: **10.1021/nl8037147**.

30 N. Chanda, V. Kattumuri and R. Shukla, *et al.*, Bombesin functionalized gold nanoparticles show *in vitro* and *in vivo* cancer receptor speci fi city, *Proc. Natl. Acad. Sci.*, 2010, **107**, 8760–8765, DOI: **10.1073/pnas.1002143107**.

31 R. Kannan, A. Zambre and N. Chanda, *et al.*, Functionalized radioactive gold nanoparticles in tumor therapy, *Wiley Interdiscip. Rev.: Nanomed. Nanobiotechnol.*, 2012, **4**(1), 42–51, DOI: **10.1002/wnan.161**.

32 M. U. Farooq, V. Novosad and E. A. Rozhkova, *et al.*, Gold Nanoparticles-enabled Efficient Dual Delivery of Anticancer Therapeutics to HeLa Cells, *Sci. Rep.*, 2018, **8**(1), 1–12, DOI: 10.1038/s41598-018-21331-y.

33 V. C. Thipe, K. P. Amiri and P. Bloebaum, *et al.*, Development of resveratrol-conjugated gold nanoparticles: interrelationship of increased resveratrol corona on anti-tumor efficacy against breast, pancreatic and prostate cancers, *Int. J. Nanomed.*, 2019, **14**, 4413–4428, DOI: 10.2147/ijn.s204443.

34 T. Ishida, T. Murayama, A. Taketoshi and M. Haruta, Importance of Size and Contact Structure of Gold Nanoparticles for the Genesis of Unique Catalytic Processes, *Chem. Rev.*, 2020, **120**(2), 464–525, DOI: 10.1021/acs.chemrev.9b00551.

35 F. Y. Kong, J. W. Zhang, R. F. Li, Z. X. Wang, W. J. Wang and W. Wang, Unique Roles of Gold Nanoparticles in Drug Delivery, Targeting and Imaging Applications, *Molecules*, 2017, **22**(9), 1445, DOI: 10.3390/molecules22091445.

36 K. V. Katti, Renaissance of nuclear medicine through green nanotechnology: functionalized radioactive gold nanoparticles in cancer therapy—my journey from chemistry to saving human lives, *J. Radioanal. Nucl. Chem.*, 2016, **309**(1), 5–14, DOI: 10.1007/s10967-016-4888-0.

37 K. V. Katti, Design and development of site directed gold nanoparticles for molecular imaging and therapy, *Trans. Am. Nucl. Soc.*, 2007, **97**, 334.

38 M. Khoobchandani, K. Katti, A. Maxwell, W. P. Fay and K. V. Katti, Laminin receptor-avid nanotherapeutic EGCg-AuNPs as a potential alternative therapeutic approach to prevent restenosis, *Int. J. Mol. Sci.*, 2016, **17**(3), DOI: 10.3390/ijms17030316.

39 M. Khoobchandani, A. Zambre, K. Katti, C. H. Lin and K. V. Katti, Green Nanotechnology from Brassicaceae, *Int. J. Green Nanotechnol.*, 2013, **1**, 194308921350947, DOI: 10.1177/1943089213509474.

40 V. C. Thipe, A. Jatar, A. R. Karikachery, K. K. Katti and K. V. Katti, Green Nanotechnology of Yucca filamentosa-Phytochemicals-Functionalized Gold Nanoparticles—Antitumor Efficacy Against Prostate and Breast Cancers, *Nanotechnol., Sci. Appl.*, 2023, **16**, 19–40, DOI: 10.2147/NSA.S437812.

41 C. P. Hans, N. Sharma, E. Downey, M. Khoobchandani, K. Katti and K. V. Katti, Mangiferin Conjugated Gold Nanoparticles Protect against the Development of Abdominal Aortic Aneurysm in an Apoe−/− Mouse Model, *JVS Vasc. Sci.*, 2022, 16–17, DOI: 10.1016/j.jvssci.2022.05.038.

42 K. V. Katti, M. Khoobchandanai, A. Y. Al-yasiri, K. K. Katti, C. Cutler, *Radioactive Gold-198 Nanoparticles In Nanomedicine: Green Nanotechnology and Radiochemical Approaches in Oncology Radioactive Gold-198 Nanoparticles*, 2017, (September).

43 T. Tangthong, T. Piroonpan and V. C. Thipe, *et al.*, Bombesin peptide conjugated water-soluble chitosan gallate—a new nanopharmaceutical architecture for the rapid one-pot synthesis of prostate tumor targeted gold nanoparticles, *Int. J. Nanomed.*, 2021, **16**(October), 6957–6981, DOI: 10.2147/IJN.S327045.

44 V. C. Thipe, M. Keyster and K. V. Katti, Sustainable Nanotechnology: Mycotoxin Detection and Protection, in *Nanobiotechnology Applications in Plant Protection*, ed. K. Abd-Elsalam and R. Prasad, 2018, DOI: 10.1007/978-3-319-91161-8.

45 N. R. S. Sibuyi, V. C. Thipe and K. Panjtan-Amiri, *et al.*, Green Synthesis of Gold Nanoparticles Using Acai Berry and Elderberry Extracts and Investigation of Their Effect on Prostate and Pancreatic Cancer Cells, *BJGP Open*, 2021, **8**, 1–8, DOI: 10.1177/1849543521995310.

46 V. Thipe, N. Hall and A. Pandurangi, *et al.*, Nano-Ayurvedic Medicine Approaches Using *Ginkgo biloba*-Phytochemicals Functionalized Gold Nanoparticles Against Breast Cancer, *Nanotechnol., Sci. Appl.*, 2024, **17**, 189–210, DOI: 10.2147/NSA.S478533.

47 V. C. Thipe, A. R. Karikachery and P. Çakılkaya, *et al.*, Green nanotechnology—An innovative pathway towards biocompatible and medically relevant gold nanoparticles, *J. Drug Delivery Sci. Technol.*, 2022, **70**, 103256, DOI: 10.1016/j.jddst.2022.103256.

48 A. H. Ferreira, F. L. N. Marques and C. C. Real, *et al.*, Green Nanotechnology Through Papain Nanoparticles: Preclinical *in vitro* and *in vivo* Evaluation of Imaging Triple-Negative Breast Tumors, *Nanotechnol., Sci. Appl.*, 2024, **17**, 211–226, DOI: 10.2147/NSA.S474194.

49 R. M. Williams, S. Chen and R. E. Langenbacher, *et al.*, Harnessing nanotechnology to expand the toolbox of chemical biology, *Nat. Chem. Biol.*, 2021, **17**(2), 129–137, DOI: 10.1038/s41589-020-00690-6.

50 H. J. Vaughan, J. J. Green and S. Y. Tzeng, Cancer-Targeting Nanoparticles for Combinatorial Nucleic Acid Delivery, *Adv. Mater.*, 2020, **32**(13), 1901081, DOI: 10.1002/adma.201901081.

51 K. V. Katti, M. Khoobchandani and V. C. Thipe, *et al.*, Prostate tumor therapy advances in nuclear medicine: green nanotechnology toward the design of tumor specific radioactive gold nanoparticles, *J. Radioanal. Nucl. Chem.*, 2018, **318**(3), 1737–1747, DOI: 10.1007/s10967-018-6320-4.

52 K. V. Katti, E. Boote and R. Kannan, *Stabilized gold nanoparticle and contrast agent*, *US Pat.*, 2017.

53 N. Chanda, P. Kan and L. D. Watkinson, *et al.*, Radioactive gold nanoparticles in cancer therapy: therapeutic efficacy studies of GA- 198 AuNP nanoconstruct in prostate tumor – bearing mice, *Nanomedicine*, 2010, **6**(2), 201–209, DOI: 10.1016/j.nano.2009.11.001.

54 V. Kattumuri, K. V. Katti, E. Boote, R. Kannan, S. Casteel and R. Churchill, *Stabilized gold nanoparticle and contrast agent*, US Pat. 9 549 998, filed 27 June 2008, issued 24 January 2017.

55 World Health Organization (WHO), General Guidelines for Methodologies on Research and Evaluation of Traditional Medicine World Health Organization, 2000.

56 World Health Organization (WHO), WHO Global Report on Traditional and Complementary Medicine 2019, 2019.

57 V. K. Singh, D. Arora, M. I. Ansari and P. K. Sharma, Phytochemicals based chemopreventive and chemotherapeutic

strategies and modern technologies to overcome limitations for better clinical applications, *Phytother. Res.*, 2019, **33**(12), 3064–3089, DOI: 10.1002/ptr.6508.

58 S. S. Parimalam, S. Badilescu, R. Bhat and M. Packirisamy, A Narrative review of scientific validation of gold- and silver-based Indian medicines and their future scope, *Longhua Chin. Med.*, 2020, **3**, 10, DOI: 10.21037/lcm-20-34.

59 M. Barve, M. Mashru, C. Jagtap, B. J. Patgiri and P. K. Prajapati, Therapeutic potentials of metals in ancient India: A review through Charaka Samhita, *J. Ayurveda Integr. Med.*, 2011, **2**(2), 55–63, DOI: 10.4103/0975-9476.82523.

60 Y. S. Jaiswal and L. L. Williams, A glimpse of Ayurveda – The forgotten history and principles of Indian traditional medicine, *J. Tradit. Complementary Med.*, 2017, **7**(1), 50–53, DOI: 10.1016/j.jtcme.2016.02.002.

61 T. Patil-Bhole, A. Wele and R. Gudi, *et al.*, Nanostructured gold in ancient Ayurvedic calcined drug 'swarnabhasma, *J. Ayurveda Integr. Med.*, 2021, **12**(4), 640–648, DOI: 10.1016/j.jaim.2021.06.017.

62 M. Xu, C. Ren and Y. Zhou, *et al.*, Enhanced macrophage polarization induced by COX-2 inhibitor-loaded Pd octahedral nanozymes for treatment of atherosclerosis, *Chin. Chem. Lett.*, 2023, **34**(1), DOI: 10.1016/j.cclet.2022.06.008.

63 J. W. Xiao, S. X. Fan, F. Wang, L. D. Sun, X. Y. Zheng and C. H. Yan, Porous Pd nanoparticles with high photothermal conversion efficiency for efficient ablation of cancer cells, *Nanoscale*, 2014, **6**(8), 4345–4351, DOI: 10.1039/C3NR06843A.

64 T. L. Bray, M. Lee, A. Serrels, M. Arruebo and N. O. Carragher, High-Precision Photothermal Ablation Using Biocompatible Palladium Nanoparticles and Laser Scanning Microscopy, *ACS Appl. Mater. Interfaces*, 2018, DOI: 10.1021/acsami.7b17282.

65 A. Dumas and P. Couvreur, Palladium: A future key player in the nanomedical field?, *Chem. Sci.*, 2015, **6**(4), 2153–2157, DOI: 10.1039/c5sc00070j.

66 S. Gurunathan, M. H. Kang, M. Qasim and J. H. Kim, Nanoparticle-mediated combination therapy: Two-in-one approach for cancer, *Int. J. Mol. Sci.*, 2018, **19**(10), 1–37, DOI: 10.3390/ijms19103264.

67 A. M. Gamal-Eldeen, D. Moustafa and S. M. El-Daly, *et al.*, Photothermal therapy mediated by gum Arabic-conjugated gold nanoparticles suppresses liver preneoplastic lesions in mice, *J. Photochem. Photobiol., B*, 2016, **163**, 47–56, DOI: 10.1016/j.jphotobiol.2016.08.009.

68 B. Salehi, A. P. Mishra, M. Nigam, B. Sener and M. Kilic, Resveratrol: A Double-Edged Sword in Health Benefits, *Biomedicines*, 2018, **6**, 91, DOI: 10.3390/biomedicines6030091.

69 C. D. Capitani, A. C. L. Carvalho, D. P. Rivelli, S. B. M. Barros and I. A. Castro, Evaluation of natural and synthetic compounds according to their antioxidant activity using a multivariate approach, *Eur. J. Lipid Sci. Technol.*, 2009, **111**(11), 1090–1099, DOI: 10.1002/ejlt.200800215.

70 Y. Sueishi, M. Ishikawa and D. Yoshioka, *et al.*, Oxygen radical absorbance capacity (ORAC) of cyclodextrin-solubilized flavonoids, resveratrol and astaxanthin as measured with the ORAC-EPR method, *J. Clin. Biochem. Nutr.*, 2012, **50**(2), 127–132, DOI: 10.3164/jcbn.11-21.

71 S. Sinha, D. McKnight and K. V. Katti, *et al.*, Gold Nanoparticles Stabilized in Gum Arabic for Corneal Gene Therapy, *Invest. Ophthalmol. Visual Sci.*, 2008, **49**(13), 4787.

72 L. Camont, C. H. Cottart and Y. Rhayem, *et al.*, Simple spectrophotometric assessment of the trans-/cis-resveratrol ratio in aqueous solutions, *Anal. Chim. Acta*, 2009, **634**(1), 121–128, DOI: 10.1016/j.aca.2008.12.003.

73 V. Nour, I. Trandafir and C. Muntean, Ultraviolet Irradiation of Trans-Resveratrol and HPLC Determination of Trans-Resveratrol and Cis-Resveratrol in Romanian Red Wines, *J. Chromatogr. Sci.*, 2012, **50**(10), 920–927.

74 K. E. Allan, C. E. Lenehan and A. V. Ellis, UV Light Stability of α -Cyclodextrin/Resveratrol Host – Guest Complexes and Isomer Stability at Varying pH, *Aust. J. Chem.*, 2009, **62**, 921–926, DOI: 10.1071/CH08506.

75 A. J. Kora and L. Rastogi, Green synthesis of palladium nanoparticles using gum ghatti (*Anogeissus latifolia*) and its application as an antioxidant and catalyst, *Arabian J. Chem.*, 2015, 9, DOI: 10.1016/j.arabjc.2015.06.024.

76 N. Using, M. E. Assal, H. Z. Alkhathlan and A. Al-warthan, Green Synthesis and Characterization of Palladium Nanoparticles Using Origanum vulgare L. Extract and Their Catalytic Activity, *Molecules*, 2017, **22**, 165, DOI: 10.3390/molecules22010165.

77 A. Sikora, D. Bartczak and D. Geißler, *et al.*, A systematic comparison of different techniques to determine the zeta potential of silica nanoparticles in biological medium, *Anal. Methods*, 2015, **7**(23), 9835–9843, DOI: 10.1039/c5ay02014j.

78 J. A. Viator, S. Gupta and B. S. Goldschmidt, *et al.*, Gold nanoparticle mediated detection of prostate cancer cells using photoacoustic flowmetry with optical reflectance, *J. Biomed. Nanotechnol.*, 2010, **6**(2), 187–191, DOI: 10.1166/jbn.2010.1105.

79 A. Castaño and M. S. Maurer, Natural history and therapy of TTR-cardiac amyloidosis: emerging disease-modifying therapies from organ transplantation to stabilizer and silencer drugs, *Heart Failure Rev.*, 2015, **20**(2), 163–178, DOI: 10.1007/s10741-014-9462-7.

80 A. Hassani, M. M. S. Azarian, W. N. Ibrahim and S. A. Hussain, Preparation, characterization and therapeutic properties of gum arabic-stabilized gallic acid nanoparticles, *Sci. Rep.*, 2020, **10**(1), DOI: 10.1038/s41598-020-71175-8.

81 S. Moradi and N. Anarjan, Preparation and characterization of α-tocopherol nanocapsules based on gum Arabic-stabilized nanoemulsions, *Food Sci. Biotechnol.*, 2019, **28**(2), 413–421, DOI: 10.1007/s10068-018-0478-y.

82 M. M. Al-Ansari, N. D. Al-Dahmash and A. J. A. Ranjitsingh, Synthesis of silver nanoparticles using gum Arabic: Evaluation of its inhibitory action on Streptococcus mutans causing dental caries and endocarditis, *J. Infect. Public Health*, 2021, **14**(3), 324–330, DOI: 10.1016/j.jiph.2020.12.016.

83 C. Ai, C. Zhao and C. Xiang, *et al.*, Gum arabic as a sole wall material for constructing nanoparticle to enhance the stability and bioavailability of curcumin, *Food Chem.: X*, 2023, **18**, DOI: 10.1016/j.fochx.2023.100724.

84 M. G. Dorrington and I. D. C. Fraser, NF-κB Signaling in Macrophages: Dynamics, Crosstalk, and Signal Integration, *Front. Immunol.*, 2019, **10**, DOI: **10.3389/fimmu.2019.00705**.

85 M. Sungu, M. Isik and Ü. Güler, *et al.*, Manipulating macrophage polarization with nanoparticles to control metastatic behavior in heterotypic breast cancer microtissues via exosome signaling, *Nanoscale*, 2023, **16**(1), 394–410, DOI: **10.1039/d3nr04980a**.

86 S. Gurunathan, M. H. Kang, M. Jeyaraj and J. H. Kim, Palladium nanoparticle-induced oxidative stress, endoplasmic reticulum stress, apoptosis, and immunomodulation enhance the biogenesis and release of exosome in human leukemia monocytic cells (Thp-1), *Int. J. Nanomed.*, 2021, **16**, 2849–2877, DOI: **10.2147/IJN.S305269**.

87 A. S. Wentzel, J. Petit and W. G. Van Veen, *et al.*, Transcriptome sequencing supports a conservation of macrophage polarization in fish, *Sci. Rep.*, 2020, 1–15, DOI: **10.1038/s41598-020-70248-y**.

88 X. Zheng, K. Turkowski and J. Mora, *et al.*, Redirecting tumor-associated macrophages to become tumoricidal effectors as a novel strategy for cancer therapy, *Oncotarget*, 2017, **8**(29), 48436–48452.

89 B. Ruffell and L. M. Coussens, Macrophages and therapeutic resistance in cancer, *Cancer Cell*, 2015, **27**(4), 462–472, DOI: **10.1016/j.ccell.2015.02.015**.

90 F. Zhang, N. N. Parayath and C. I. Ene, *et al.*, Genetic programming of macrophages to perform anti-tumor functions using targeted mRNA nanocarriers, *Nat. Commun.*, 2019, **10**(1), 3974, DOI: **10.1038/s41467-019-11911-5**.

91 N. Joudeh, A. Saragliadis, G. Koster, P. Mikheenko and D. Linke, Synthesis methods and applications of palladium nanoparticles: A review, *Front. Nanotechnol.*, 2022, **4**, DOI: **10.3389/fnano.2022.1062608**.

92 P. G. Cavalcante de Freitas, B. Rodrigues Arruda and M. G. Araújo Mendes, *et al.*, Resveratrol-Loaded Polymeric Nanoparticles: The Effects of D-α-Tocopheryl Polyethylene Glycol 1000 Succinate (TPGS) on Physicochemical and Biological Properties against Breast Cancer *In Vitro* and *In Vivo*, *Cancers*, 2023, **15**(10), DOI: **10.3390/cancers15102802**.

93 S. Wang, J. Li and M. Chen, *et al.*, Palladium nanoplates scotch breast cancer lung metastasis by constraining epithelial-mesenchymal transition, *Natl. Sci. Rev.*, 2021, **8**(7), DOI: **10.1093/nsr/nwaa226**.

94 Y. Liu, J. Li, M. Chen, X. Chen and N. Zheng, Palladium-based nanomaterials for cancer imaging and therapy, *Theranostics*, 2020, **10**(22), 10057–10077, DOI: **10.7150/thno.45990**.

